UNIVERSITY OF CALIFORNIA

SANTA CRUZ

MULTISTABILITY, IONIC DOPING, AND CHARGE DYNAMICS IN ELECTROSYNTHESIZED POLYPYRROLE, POLYMER-NANOPARTICLE BLEND NONVOLATILE MEMORY, AND FIXED *P-I-N* JUNCTION POLYMER LIGHT-EMITTING ELECTROCHEMICAL CELLS

A dissertation submitted in partial satisfaction of the
requirements for the degree of

DOCTOR OF PHILOSOPHY

in

PHYSICS

by

Daniel Theodore Simon

June 2007

The Dissertation of Daniel Theodore Simon
is approved:

Professor Sue Carter, Chair

Professor Frank Bridges

Doctor J. Campbell Scott

Lisa C. Sloan
Vice Provost and Dean of Graduate Studies

Table of Contents

List of Figures

List of Tables

Abstract

Multistability, Ionic Doping, and Charge Dynamics in Electrosynthesized Polypyrrole, Polymer-Nanoparticle Blend Nonvolatile Memory, and Fixed *p-i-n* Junction Polymer Light-Emitting Electrochemical Cells

by

Daniel Theodore Simon

A variety of factors make semiconducting polymers a fascinating alternative for both device development and new areas of fundamental research. Among these are solution processability, low cost, flexibility, and the strong dependence of conduction on the presence of charge compensating ions. With the lack of a complete fundamental understanding of the materials, and the growing demand for novel solutions to semiconductor device design, research in the field can take many, often multifaceted, routes.

Due to ion-mediated conduction and versatility of fabrication, conducting polymers can provide a route to the study of neural signaling. In the first of three research topics presented, junctions of polypyrrole electropolymerized on microelectrode arrays are demonstrated. Individual junctions, when synthesized in a three-electrode configuration, exhibit current switching behavior analogous to neural weighting. Junctions copolymerized with thiophene exhibit current rectification and the nonlinear current-voltage behavior requisite for complex neural systems. Applications to larger networks, and eventual use in analysis of signaling, are discussed.

In the second research topic, nonvolatile resistive memory consisting of gold nanoparticles embedded in a polymer film is examined using admittance spectroscopy. The frequency

dependence of the devices indicates space-charge-limited transport in the high-conductivity "on" state, and similar transport in the lower-conductivity "off" state. Furthermore, a larger dc capacitance of the on state indicates that a greater amount of filling of midgap trap levels introduced by the nanoparticles increases conductivity, leading to the memory effect. Implications on the question as to whether or not the on state is the result of percolation pathways is discussed.

The third and final research topic is a presentation of enhanced efficiency of polymer light-emitting electrochemical cells (LECs) by means of forming a doping self-assembled monolayer (SAM) at the cathode-polymer interface. The addition of the SAM causes a twofold increase in quantum efficiency. Photovoltaic analysis indicates that the SAM increases both open-circuit voltage and short-circuit current. Current versus voltage data are presented which indicate that the SAM does not simply introduce an interfacial dipole layer, but rather provides a fixed doping region, and thus a more stable *p*-*i*-*n* structure.

Acknowledgments

A great many people contributed to my ability to complete the research detailed in this manuscript. In all honesty, the entire Sue Carter research group – past and present – could be credited as co-authors to all of my work. Most importantly among them were Janelle Leger, for an unceasing ability to doubt my explanations, thereby forcing me to either make them stronger or change my mind, and Mike Griffo, for a steady stream of ideas and insights into *all* aspects of our lab and our research. For my introduction to the analytical techniques used in Chap. 5, and indeed much of my research in Sue Carter's lab, I owe a great deal to Glenn Alers. His expertise and industrial perspective were greatly appreciated. Many thanks are also due to J. Campbell Scott, for consistently taking time to help and lend a true master's insight at a moment's notice, and Luisa Bozano, for a wide range of help, advice, and technical assistance. I would also like to thank Bud Bridges for his advice and guidance in the writing of this manuscript.

Naturally, none of this would have been possible without the aid of my advisor, Sue Carter. Throughout my time in her tutelage, she seemed to give me just the right insights, just the right pushes, as well as just the right freedom and trust, to guide my own intellectual movement in exciting and enlightening directions. She has truly passed a mighty torch to me.

On a personal note, my wife Rozalyn was absolutely invaluable in my ability to complete this endeavor. Her intellectual and emotional support and encouragement, coupled with her love and patience, enabled me to excel at my research while maintaining a healthy perspective on the "big picture" of what I was attempting to accomplish. Finally, and by no means least

in this honored company, my daughter Adeline led me to discover anew what it is to learn and what it is to teach.

Disclaimers

Figures 2.1 and 2.2 were generated using the GAMESS *ab-initio* quantum chemistry package,[†] and the MacMolPlt visualization program.[‡] Chapters 4, 5, 6, and the abstract[§] of this dissertation include previously published material (with stylistic modifications to the graphics):

Chapter 4:
Daniel T. Simon and Sue A. Carter. Electrosynthetically patterned conducting polymer films for investigation of neural signaling. *Journal of Chemical Physics* **124**, 204709 (2006).
D. T. Simon's contribution: All research and all writing.

Chapter 5:
Daniel T. Simon, Michael S. Griffo, Richard A. DiPietro, Sally A. Swanson, and Sue A. Carter. Admittance spectroscopy of polymer-nanoparticle non-volatile memory devices. *Applied Physics Letters* **89**, 133510 (2006).
D. T. Simon's contribution: Majority of research and majority of writing (both with M. S. G.).

Chapter 6:
Daniel T. Simon, David B. Stanislowski, and Sue A. Carter. Fixed *p-i-n* junction polymer light-emitting electrochemical cells based on charged self-assembled monolayers. *Applied Physics Letters* **90**, 103508 (2007).
D. T. Simon's contribution: Majority of research (with D. B. S.) and all writing.

Professor Sue A. Carter directed and supervised the research which forms the basis for this dissertation. The material listed above is reprinted with permission of all co-authors and the original publisher.[¶]

[†] M.W. Schmidt *et al. Journal of Computational Chemistry* **14**, 1347 (1993).
[‡] B.M. Bode and M.S. Gordon. *Journal of Molecular Graphics and Modelling* **16**, 133 (1998).
[§] The abstracts of the original articles were paraphrased.
[¶] See first page of said chapters for full copyright acknowledgment and digital object identifier (DOI) numbers.

Chapter 1

Introduction

The twentieth century will certainly be remembered as the dawn of thermoplastic polymers, or as we all know them, plastics. While research in the later half of the nineteenth century on precursor materials laid the groundwork, this unprecedented introduction into our culture of a completely man-made material[†] began in 1907, when Leo Baekeland created Bakelite, the first synthetic polymer.[1] Bakelite and its technological descendants were primarily used as electrical insulators. Indeed, it was not until several decades later that researchers discovered that π-conjugated hydrocarbon polymers such as polyacetylene and polypyrrole (Fig. 1.1) could be made semiconducting.[2,3] By exposure to specific halogen vapors, mobile electronic distortions along the polymer's backbone could be generated and stabilized, thus contributing to a current and drastically increasing the conductivity. This discovery garnered the Nobel Prize in Chemistry for Alan MacDiarmid, Alan Heeger and Hideki Shirakawa in 2000.

While the success of creating semiconducting polymers was monumental, the practical value of such materials, which required an ornate series of synthetic steps, was minimal. Furthermore, the goal of increasing the conductivity into the metallic range was found to be (at

[†]There had been previous plastic materials, but all had been based on natural sources, *e.g.*, celluloid, based on cellulose and camphor.

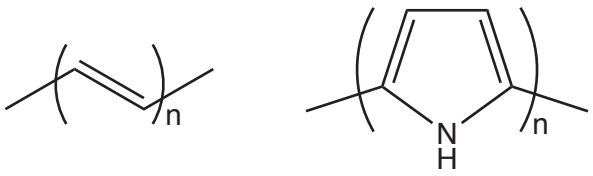

(a) **(b)**

Figure 1.1: (a) Polyacetylene and (b) polypyrrole: the first semiconducting polymers. Note the alternating single and double bonds creating the π-conjugated backbone.

least initially) unattainable. Research proceeded then on understanding the mechanism of conduction in these new materials. Throughout the 1980s, soliton and polaron excitations became the accepted model for semiconductivity in π-conjugated polymers.[4,5] In conjunction with this newfound fundamental understanding, developments in polymer synthesis and solubility – most notably polypyrrole, polythiophene, and poly(phenylene vinylene) and their derivatives – paved the way for a major push in the direction of device development. Polymer-based light-emitting diodes (LEDs),[6,7] solar cells,[8] and transistors[9,10] were successfully demonstrated. However, the viability of these devices as competition with the concurrently advancing complimentary metal oxide-semiconductor (CMOS) industry remained – and still remains in many cases – always "just around the corner".

The great hopes for conducting polymer-based alternatives to – or incorporation within – CMOS technologies is not unfounded. Most importantly, the plastic nature of these materials opens up the possibility for flexible electronics. Also, since these materials can be deposited from solution, rather than the more costly and defect-susceptible techniques required for CMOS technologies, there is a potential for significant cost reduction. For example, a basic polymer LED can be made by simply spinning a conducting polymer dissolved in organic solvent onto

indium-tin-oxide patterned glass, and evaporating a suitable metallic top electrode; this is done *without* the necessity of a clean room. On the other hand, fabrication of an analogous inorganic-based LED (*e.g.*, indium gallium arsenide devices) would require much more elaborate – and expensive – equipment for deposition of the emissive layer, and this process *would* necessitate a clean room. However, as hinted above, there is a trade-off: the inorganic-based LED would far outperform the simple polymer device.

The difficulty in both understanding the basic mechanisms of conducting polymers and bringing to market truly competitive alternatives to entrenched CMOS technologies, coupled with the unique properties and evident promise of the conducting polymer platform, has maintained the interest of a great many research groups worldwide over the past few decades.[†] This effort has generally taken two basic approaches. The first approach lies in the optimization of basic devices such as LEDs, transistors, and solar cells. This work has focused on both a deeper fundamental understanding, and an attempt to develop highly efficient polymer-based alternatives (or counterparts) to existing technologies. The second major research effort has been to develop an understanding of, and applications for, the various truly unique aspects of conducting polymers. For example, the ion-mediated conduction of polymers can be developed into an ion sensitive device rather easily. In this case, the two schools of research are naturally intertwined: developments in the basic understanding of charge transport will impact *all* branches of the field; or a new type of device may shed light on ionic doping physics applicable to a wide range of devices, *e.g.*, transistors. The research presented in Chap. 4 is on just such a system.

[†]A search on the Web of Science (http://isiknowledge.com) yields over 3800 articles published in the last ten years with "conducting polymer" in the title, abstract, or keywords.

Table 1.1: Benefits and associated drawbacks of conducting polymers for device development. Also shown are comparisons to existing complementary metal-oxide semiconductor (CMOS) or general inorganic technologies. The last three columns detail which of these material aspects were motivation for the research documented in Chaps. 4, 5, and 6.

CP Benefit	Drawback	CMOS Comparison	Ch. 4	Ch. 5	Ch. 6
Solution processable		Not possible	✓	✓	✓
2-3 eV energy gap		Comparable			✓
Synthesizable *in situ*	Difficult to incorporate into fabrication	Requires prefab. substrates	✓		
Potential for CMOS integration		n/a		✓	✓
Impedance response to molecular "dopants"	Potentially slow	Impermeable to molec. dopants	✓		✓
Flexible		Inherently rigid	✓	✓	✓
Robust against defects	Susceptible to oxidative degradation	Very susceptible		✓	✓
Low-cost fabrication	Undetermined at high-throughput	Costly, but already established		✓	✓

Being a rather young field, and existing at a unique crossroads of condensed matter physics, chemical engineering, materials science, and device development, research on conducting polymers is necessarily interdisciplinary. However, there have arisen rather canonical routes into the field – *i.e.*, there exist a handful of significant benefits of polymer-based electronics that are put forward as justification for research and development. Some of these are listed in Table 1.1 along with associated drawbacks and comparisons of these benefits to existing CMOS technology. Also listed in the table are the applicability of these aspects to the motivation behind the research documented below in Chaps. 4, 5, and 6.

Specifically, Chap. 4 deals with the use of polypyrrole films electrosynthetically patterned on a microscopic scale for use in the modeling and analysis of neural signaling. As seen in Table 1.1, this research was motivated by both the strong dependence of the impedance to changes in local ion concentration, and the ability to synthesize certain polymers *in situ*. The

aim of this research was to demonstrate signal "weighting" and nonlinear transport analogous to that seen in both biological and algorithmic neurons. Results and discussion are presented which show that this behavior can indeed be observed in these simple polymer junctions, and how these systems could be extended to larger networks.

Chap. 5 switches focus to transport properties in devices based on a blend of a conducting polymer with monolayer-protected Au nanoparticles. The motivation here was based on the demonstration that these types of structures exhibit a bistable current versus voltage effect,[11–13] directly applicable to nonvolatile resistive memory applications. Obviously, this research, in comparison to the more novel structures presented in Chap. 4, is on a structure that is in direct competition with CMOS technology, *e.g.*, flash memory, where both cost and speed are crucial. While the bistable effect was well documented – in both polymer and inorganic structures[14] – the mechanism remained a mystery: was the increased current state due to formation of filaments, or was it based on changes in charge kinetics? The material presented below documents analysis of this memory structure using admittance spectroscopy to elucidate the dynamics of injected and stored charge. Results are shown which indicate non-filamentary behavior, most likely due to the build up of trapped charge on the nanoparticles.

Chap. 6 again switches focus, this time toward the electroluminescent and electrochemical (ionic) doping properties of conducting polymers. Since the first demonstration of electroluminescence in conducting polymers,[6] significant research has been devoted to the development of viable light-emitting devices. To date, the best polymer-based LEDs fall short in light output and/or lifetime in comparison with their inorganic counterparts. Of the several proposals for improvement of this situation, light-emitting electrochemical cells (LECs)[15]

show promise in both performance and integrability with device production. These systems, described in detail below, suffer from being dynamic in nature, due to the motion of embedded ionic species within the emissive layer. In Chap. 6, a new LEC structure based on ionic dopants covalently anchored by self-assembly is proposed. Analysis of light emission and photovoltaic response are shown, and increased device performance is demonstrated.

Together, the research presented in these chapters is meant to show both specific insights into the mechanisms and dynamics, and unique device applications for conducting polymers. Rather than closing doors by answering the proposed questions, each of the topics presented below *opens* a multitude of doors into novel uses and developments by answering just these questions – and, of course, asking new ones.

In preparation for the presentation of new research, Chap. 2 introduces the reader to the underlying theories of conduction, ionic doping, light-emission, etc., in conducting polymers. Chap. 3 introduces the reader to the experimental techniques employed in the research to follow. App. A contains a list of symbols and acronyms used, App. B contains a brief discussion of the general purpose interface bus (GPIB) system used to acquire digital measurements, and App. C contains a sample of the type of software developed and used to take these measurements.

References

[1] L. H. Baekeland. Method of making insoluble products of phenol and formaldehyde. *U.S. Patent Number 942699* (7 December 1909).

[2] R. McNeill, R. Siudak, J. Wardlaw, and D. Weiss. Electronic conduction in polymers. i. the chemical structure of polypyrrole. *Australian Journal of Chemistry* **16**, 1056 (1963).

[3] C. K. Chiang, J. C. R. Fincher, Y. W. Park, A. J. Heeger, H. Shirakawa, E. J. Louis, S. C. Gau, and A. G. MacDiarmid. Electrical conductivity in doped polyacetylene. *Physical Review Letters* **39**, 1098 (1977).

[4] W. P. Su, J. R. Schrieffer, and A. J. Heeger. Soliton excitations in polyacetylene. *Physical Review B* **22**, 2099 (1980).

[5] A. J. Heeger, S. Kivelson, and J. Schrieffer. Solitons in conducing polymers. *Reviews of Modern Physics* **60**, 781 (1988).

[6] J. H. Burroughes, D. D. C. Bradley, A. R. Brown, R. N. Marks, K. Mackay, R. H. Friend, P. L. Burns, and A. B. Holmes. Light-emitting diodes based on conjugated polymers. *Nature* **347**, 539 (1990).

[7] R. H. Friend, R. W. Gymer, A. B. Holmes, J. H. Burroughes, R. N. Marks, C. Taliani, D. D. C. Bradley, D. A. D. Santos, J. L. Bredas, M. Logdlund, and W. R. Salaneck. Electroluminescence in conjugated polymers. *Nature* **397**, 121 (1999).

[8] C. J. Brabec, N. S. Sariciftci, and J. C. Hummelen. Plastic solar cells. *Advanced Functional Materials* **11**, 15 (2001).

[9] H. Koezuka and S. Etoh. Schottky barrier type diode with an electrochemically prepared copolymer having pyrrole and n-methylpyrrole units. *Journal of Applied Physics* **54**, 2511 (1983).

[10] G. Horowitz. Organic field-effect transistors. *Advanced Materials* **10**, 365 (1998).

[11] L. P. Ma, J. Liu, and Y. Yang. Organic electrical bistable devices and rewritable memory cells. *Applied Physics Letters* **80**, 2997 (2002).

[12] L. D. Bozano, B. W. Kean, V. R. Deline, J. R. Salem, and J. C. Scott. Mechanism for bistability in organic memory elements. *Applied Physics Letters* **84**, 607 (2004).

[13] L. D. Bozano, B. W. Kean, M. Beinhoff, K. R. Carter, P. M. Rice, and J. C. Scott. Organic materials and thin-film structures for cross-point memory cells based on trapping in metallic nanoparticles. *Advanced Functional Materials* **15**, 1933 (2005).

[14] J. G. Simmons and R. R. Verderber. New conduction and reversible memory phenomena in thin insulating films. *Proceedings of the Royal Society of London, Series A* **301**, 77 (1967).

[15] Q. Pei, G. Yu, C. Zhang, Y. Yang, and A. J. Heeger. Polymer light-emitting electrochemical cells. *Science* **269**, 1086 (1995).

Chapter 2

Conduction and Optical Activity in Conjugated Polymers

2.1 π-Conjugation

The hallmark of modern semiconducting – or simply "conducting"[†] – polymers is a π-conjugated backbone. This is essentially a path along the polymer consisting of carbon atoms with alternating single and double bonds (Fig. 2.1). With six electrons in its neutral state, the ground state electronic configuration of carbon is $1s^2 2s^2 2p^2$. According to orbital hybridization theory,[1] bonding between carbons entails the superposition of the valence electrons such that "hybrid" orbitals are energetically favored. In the case of carbon, one of the 2s electrons gets promoted to the 2p level leaving one 2s and three 2p electrons. Two of the 2p electrons and the lone 2s combine to form three sp^2 hybrid orbitals, leaving a lone, unhybridized $2p_z$ orbital. The three sp^2 orbitals occupy a plane with orbital separation of 120°, and the lone p_z orbital is situated perpendicular to this plane. In Fig. 2.1, the sp^2 plane is the plane of the page, and the lone p_z orbitals originating at each carbon are pointing out of (and into) the page.

[†]While π-conjugated polymers are technically semiconducting due to their finite HOMO-LUMO energy gap (discussed below), they are often referred to as "conducting" polymers. In accordance with the literature, and with apologies to the reader, these two names will be interchanged throughout this manuscript.

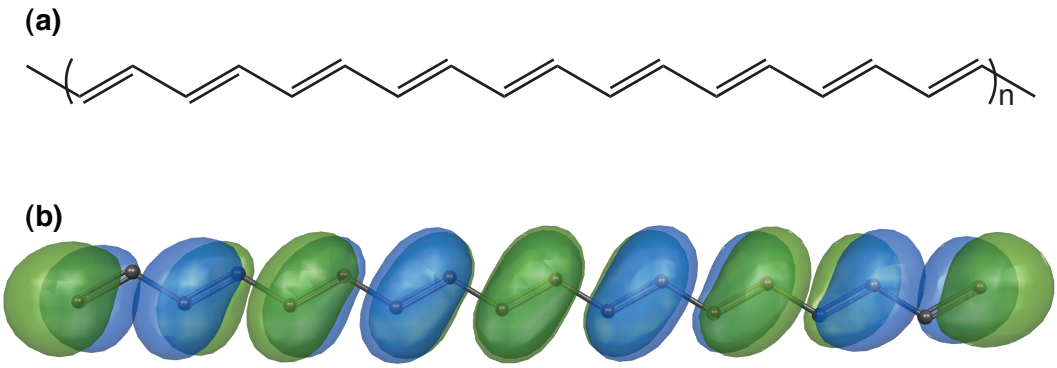

Figure 2.1: π-conjugation in the conducting polymer PA. (a) Simplified chemical structure. (b) Visualization of $\sim$90% occupancy isosurface of the highest occupied molecular orbital (HOMO) composed of superposed p_z atomic orbitals. Note that the distortion of the orbital lobes at either end of the polymer is due to the small number of repeat units used in the calculation. In this and following such visualizations, the green and blue lobes indicate opposing polarity of the electron wavefunction.

Moving the perspective from the individual carbon atoms to the molecule at large, molecular orbital theory[2] allows for the description of the inter-atomic superposition of orbitals. According to this theory, a single C$-$C bond consists of the overlap of one of the three sp^2 orbitals from each carbon. This creates what is called a σ bond. In a double C=C bond, in addition to the σ bond, there is an overlapping of the two unhybridized $2p_z$ orbitals from each carbon, resulting in what is called a π bond (Fig. 2.2a). This is the essence of the π-conjugated system: a molecule entirely or in part characterized by a chain of carbon atoms with alternating σ (single) and $\sigma+\pi$ (double) carbon bonds.

2.2 The Origin of Semiconduction

When one considers a long chain of π-conjugated carbon atoms, *e.g.*, PA (Fig. 2.1), the averaged occupancy of electrons in each carbon's lone $2p_z$ orbital is one. That is, each

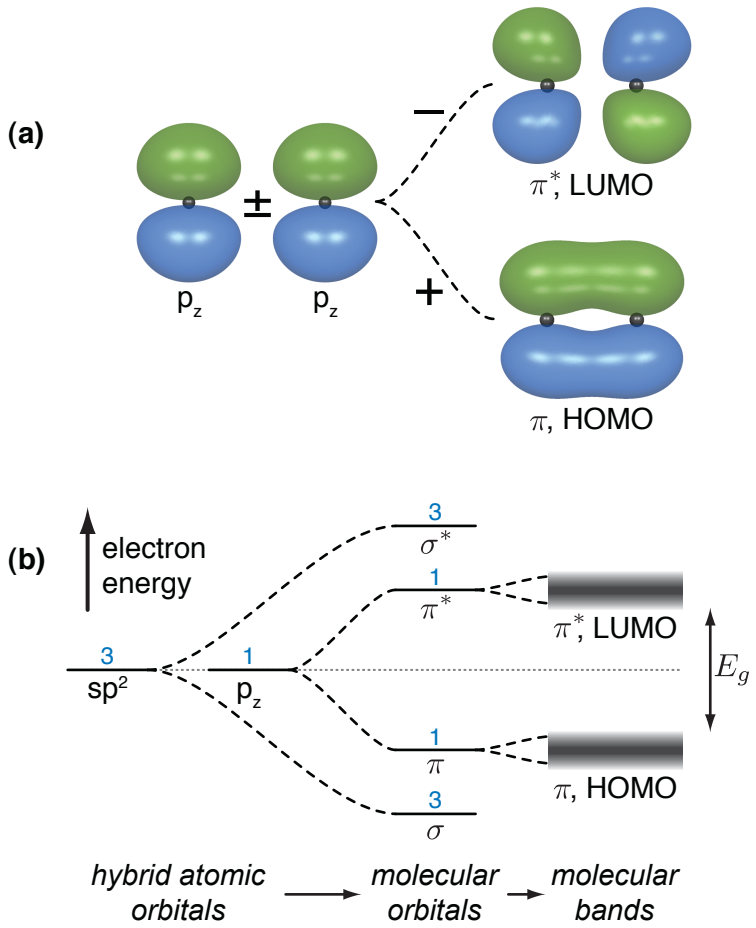

Figure 2.2: Hybridization of the atomic orbitals/energies of carbon. (a) Hybridization of two $2p_z$ orbitals showing isosurfaces containing ∼90% probability. Symmetric superposition (addition) of the two p_zs leads to the lower energy π level. Antisymmetric superposition (subtraction) leads to the higher energy π^*. (b) Energy level diagram showing the energy level splitting giving rise to the band gap energy, E_g. The blue numbers over each level indicate the spatial degrees of freedom.

carbon's $2p_z$ orbital is only half filled. This, of course, is the definition of a metallic conductor: a system in which the Fermi energy, E_f, lies within a region of accessible energies, in this case at the 2p energy level. If this were the case with π-conjugated systems, instead of alternating single and double bonds, the carbon chain would consist of symmetric bonds on either side of

each carbon, each with "1.5" bonds, with the simplest unit being a single C=C.[†] The bonds would be of equal length, electrons would be delocalized along the length of the π-conjugation, and one would have a one-dimensional metallic conductor.

However, this is not the case. Due to the Peierls instability,[3] this would-be one-dimensional conductor collapses into a dimerized state where each C=C=C unit relaxes to C−C=C, *i.e.*, the "1.5" bonds supporting conduction collapse into alternating single and double bonds. This relaxation splits the $2p_z$ energy level (equal to E_f) into two new levels spaced equidistant above and below E_f: the π and π^* energies. The multitude of π and π^* levels along the entire polymer, and the small variability in these energies due to local charge distortions, solvents, etc., create the π and π^* energy *bands* corresponding to long range molecular orbitals. While this combination of discrete levels into bands is true for all levels (*e.g.*, the σ and σ^* levels, spaced below and above the π and π^*), it is the π and π^* bands which define the highest occupied molecular orbital (HOMO) and lowest unoccupied molecular orbital (LUMO), as seen in Fig. 2.2.

The HOMO-LUMO energy gap, E_g, is completely analogous to the valence-conduction gap in crystalline and inorganic semiconductors (*e.g.*, silicon). For conducting polymers, E_g is often in the range of 2-3 eV, which is equivalent to the wavelength range 413-620 nm (cf. Sec. 2.6). Owing to the fact that 0 eV $< E_g \lesssim$ 4.5 eV,[‡] these polymers behave as electrical semiconductors (cf. footnote on pg. 9).

[†]Recall that there are two electrons within each bond. Here the σ bond is filled with two electrons, and the π bond only has one, so the 1.5 bond actually consists of three electrons.

[‡]The 4.5 eV cutoff between materials classified as semiconductors or as insulators is rather arbitrary, but refers to the ability for low energy excitations (thermal, photoexcitation, etc.) to populate the LUMO or conduction band.

2.3 The Mechanism of Semiconduction

In metals and crystalline semiconductors the periodicity of the material supports conduction via macroscopically delocalized electrons. Conducting polymers, on the other hand, are amorphous by nature: the "spaghetti" structure of multitudes of interwoven polymer strands of varying length is anything but periodic.[†] Following their seminal experiments on conducting PA,[4] Wu Pei Su and Alan Heeger, collaborating with Robert Schrieffer, published a theoretical explanation of conduction in PA.[5] They posited that electronic structure deformations of the π-conjugated backbone were the charge carriers. Specifically, p_z orbitals taken out of π hybridization could become oxidized or reduced and subsequently stabilized by ions of opposite charge. They termed the electronic structure deformations "solitons" since each is essentially a "moving domain wall" between degenerate structures on either side (shifting the double bonds in PA by one carbon results in an energetically degenerate structure). A summary of this mechanism is shown in Fig. 2.3.

In the case of non-degenerate polymers, the mechanism is quite similar, but the charge carriers are slightly more complex than p_z-radical domain walls. In the case of PPy (Fig. 2.4), a single p_z orbital taken out of π-conjugation, and the resulting shift of bonds, results in a large region of the polymer being raised into a higher energy state. Without further modification of the electronic stucture, the lone p_z would snap back into π-conjugation, and the system would relax. However, if another p_z within the higher energy region is taken out of π-conjugation, the bulk of the polymer can return to the ground state, while a small region is left in the excited (bond

[†]There have been numerous efforts to better organize polymer conductors, *e.g.*, regio-regular poly(3-hexylthiophene) (P3HT), but the accepted mechanisms are still based on a basically amorphous material.

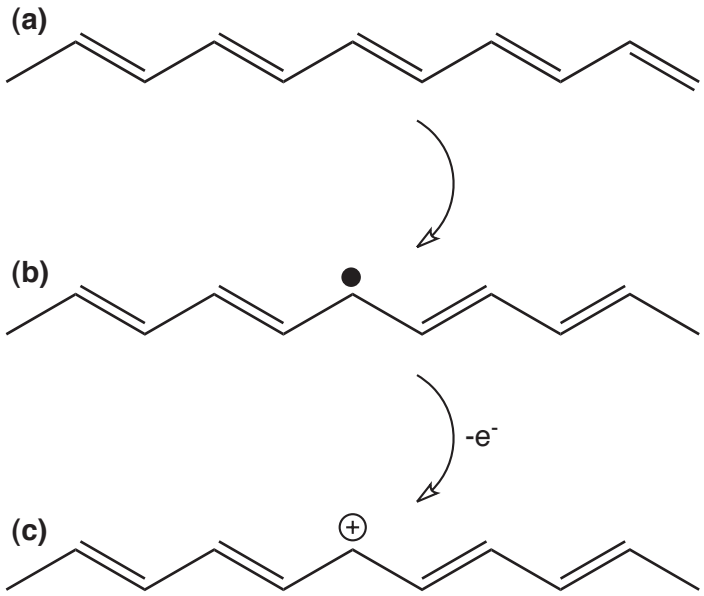

Figure 2.3: Route to positive soliton formation in the degenerate polymer PA. (a) Neutral PA in the ground state. (b) Single, neutral p_z taken out of π-conjugation, resulting in soliton domain wall between ground state regions. (c) Oxidation of the soliton resulting in positive charge carrier. The situation for negative solitons is analogous.

shifted) state as the domain wall between ground state regions. Single or double oxidation (or reduction) results in the formation of the charge carrier: a polaron (single redox) or bipolaron (double redox). This scheme is summarized in Fig. 2.4. The structural distortion (not shown in the figure) of the polaron arises from the fact that single bonds are slightly longer than double bonds, leading to a modification of the ring geometries. For other non-degenerate ground state conducting polymers, such as PPV or PT derivatives, the mechanism of charge carrier creation is identical.

The questions still remain: how exactly is the polymer oxidized or reduced into its conductive state, and how is the excited charge deformation stabilized? These questions can be answered in many ways, relating to the historical development of conducting polymer device

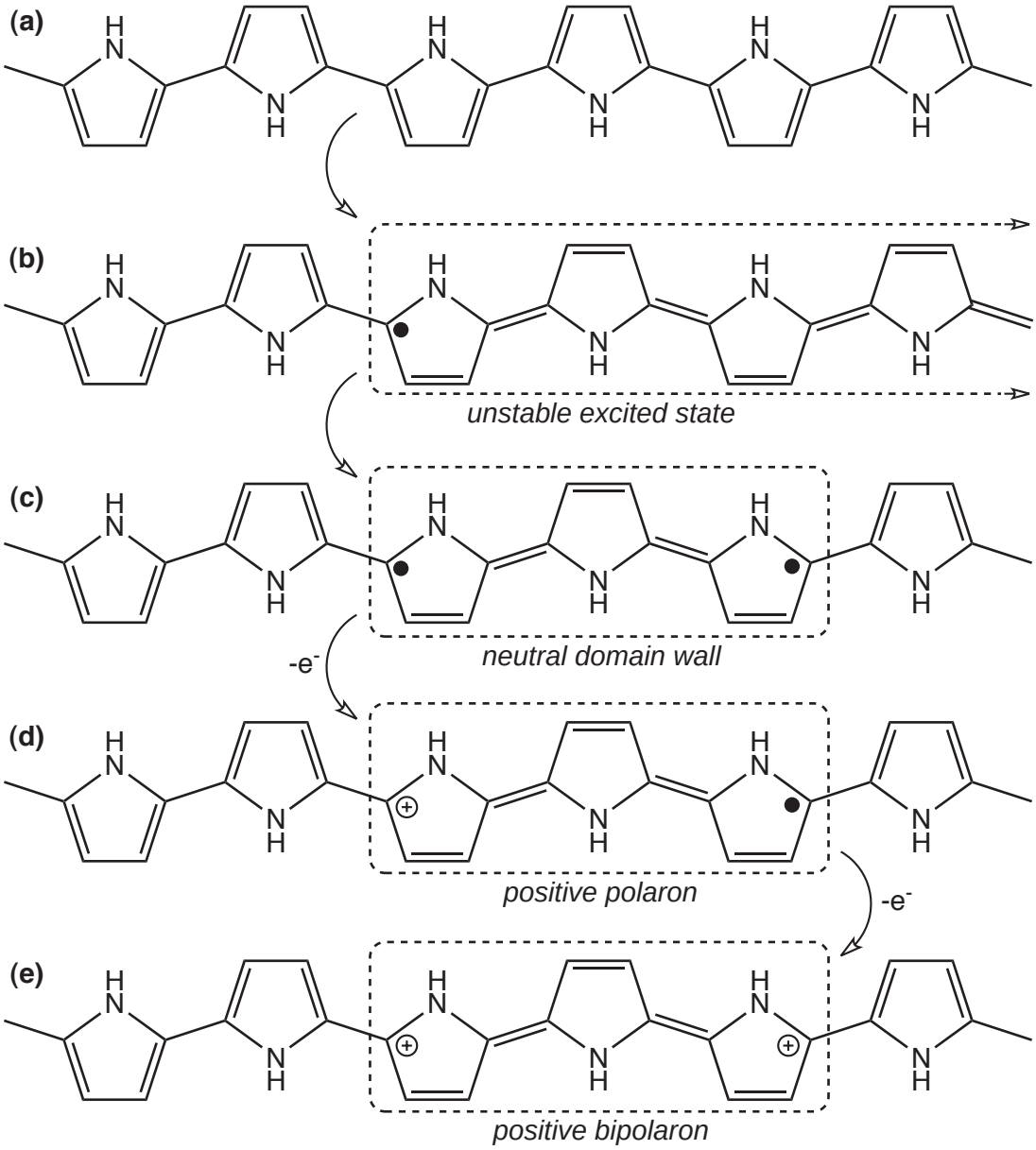

Figure 2.4: Route to positive polaron and bipolaron formation in the non-degenerate polymer PPy. (a) Neutral PPy in the ground state. (b) Single localized neutral p_z radical taken out of π-conjugation, resulting in right half of polymer in unstable excited state. (c) Two neutral p_z orbitals taken out of π-conjugation, resulting in stable domain wall between ground state regions. (d) Oxidation of domain wall resulting in positive polaron. (e) Second oxidation of polaron resulting in positive bipolaron. The situation for negative polarons is analogous.

physics. Originally,[4,6,7] the redox of the polymer was performed by the incorporation of dopant molecules into a film of polymer. Specifically, charge transfer from the neutral soliton to a dopant molecule results in a either *p*-doping (addition of mobile positive charge via oxidation of the polymer) or *n*-doping (addition of mobile negative charge via reduction) and a charged "counterion". Following Refs. 4 and 8, the process for *p*-doping PA by incorporation of iodine gas would be:

$$[\mathrm{CH}]_n \; + \; (3x/2)\,\mathrm{I}_2 \;\; \rightarrow \;\; [\mathrm{CH}]_n^{+x} \; + \; x\mathrm{I}_3^{-}\,, \tag{2.1}$$

where x is the doping level. In this mechanism, the electron removed between parts (b) and (c) of Fig. 2.3 is transferred to the neutral I_2 molecule. The result is the positive soliton of Fig. 2.3c and an I_3^- counterion. The counterion acts not only as the cause of doping, but also as a stabilizer of the positive soliton charge carrier. The case for chemical doping of non-degenerate ground state polymers is completely analogous: the oxidation or reduction of the domain wall by molecular dopants results in – and stabilizes – charged (bi)polarons (cf. Fig. 2.4).

Since the initial discoveries of conduction, the means of attaining increased conductivity have evolved somewhat. These more recent methods include refined electrochemical doping, direct injection of charge at an electrode interface, and photogeneration of charge. Some of these methods that are applicable to the research in this manuscript are discussed below.

2.4 Electrochemical Doping

As shown in the seminal research[5,6] on conducting PA and PPy, charged species (*i.e.*, ions) can play an important role in the ability of polymers to conduct. For the case of PA,

Eqn. 2.1 and the discussion above illustrate such a role for neutral and charged iodine. In more recent years, such "electrochemical doping" has been explored by blending salts within a solid polymer layer.[†] This blending takes two general forms: first, incorporation of doping ions during the synthesis stage of the polymer, and second, physical mixing in solution phase with already-synthesized polymers.

Incorporation of doping ions during synthesis entails starting with monomer units and selected salts, and synthesizing the doped polymer in a single step. The prototypical example of this technique is illustrated in the work of Diaz *et al.*,[7] where PPy was electrosynthesized in solution with a variety of dopant ions using three-electrode electrochemistry (cf. Sec. 3.2 for details of this technique). In their research, pyrrole monomer and the salt tetra-*n*-butylammonium tetrafluoroborate ($TBABF_4$) were used to polymerize conducting PPy galvanostatically. The PPy forms at the anode (working electrode) by removal of electrons, leading to radicals on adjacent monomer units which then bond to PPy, releasing H^+ (and thus H_2 gas). The radicals caused by extraction of electrons into the anode also create positive (bi)polarons which can be stabilized by BF_4^- counterions in solution (Fig. 2.5). The resulting PPy film coating the anode is then in a high-conductivity state, which depends highly on the presence of the doping counterions. Removal of these ions reduces conductivity, and vice versa. Indeed, this behavior is explored in great detail in Chap. 4 below. Furthermore, this method can be used for a wide variety of monomer units – most notably PPy and PT derivatives – so long as their oxidation potential is sufficiently low for electrons to be removed as described above.

[†]The results for PA exposed to iodine (Ref. 5) dealt with exposure to iodine gas *after* formation of the PA film.

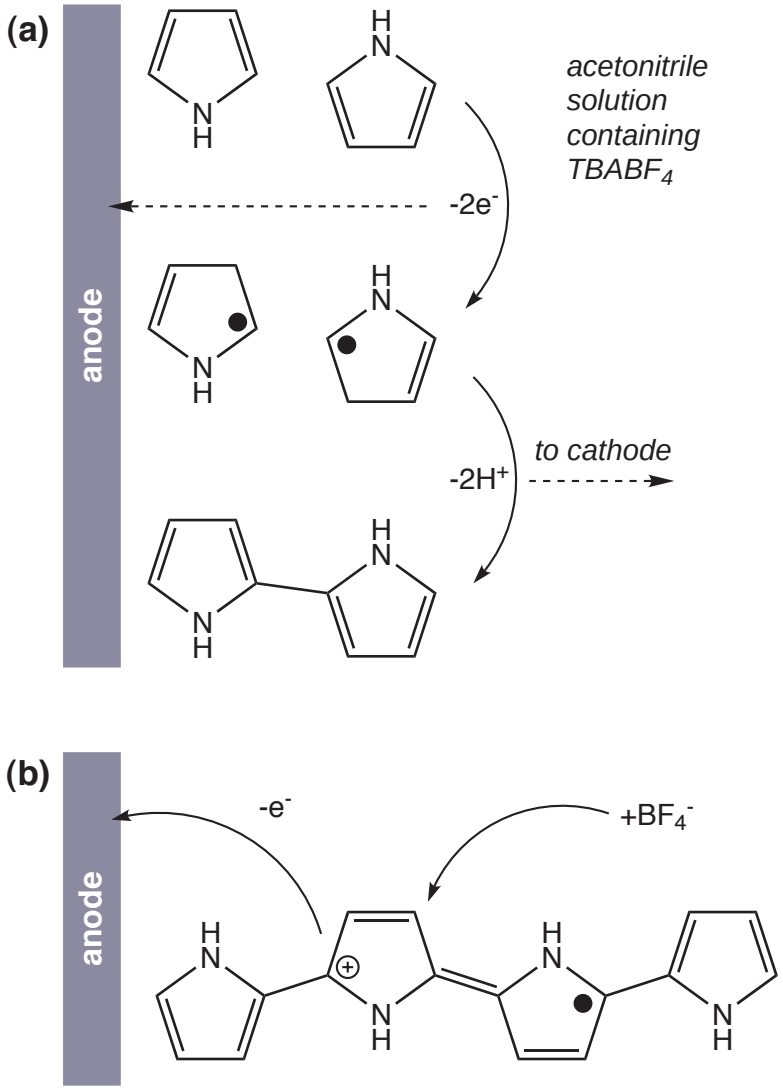

Figure 2.5: Electrochemical synthesis and doping of PPy. (a) Mechanism following Ref. 7. Py monomer is oxidized, leaving a neutral p_z radical on each ring. The radicals from two rings covalently bond (releasing H^+ and H_2) to form PPy. (b) Further oxidation of the polymer results in formation of a positive polaron (*p* doping) that is then stabilized by a BF_4^- ion in solution. Note that both (a) and (b) are parts of a solution-phase three-electrode experiment.

The second method, physical mixing of dopants with already-synthesized polymers, is most commonly used when the desired result is a solid-state thin film device of some sort. A common example of this type of electrochemical doping by mixing is seen in light-emitting

electrochemical cells (LECs) (Ref. 9 and Chap. 6). In this type of device, the conducting polymer and doping salt are included in the same solution, and it is this single solution which is used to fabricate the thin film. When a voltage bias is applied across the film, the ions dissociate and migrate toward the electrodes: cations toward the cathode, and anions toward the anode (this is discussed in the next section, particularly in Fig. 2.8b). Oxidation of the polymer at the anode is stabilized by the presence of the anions, and the the polymer is effectively *p*-doped (and vice versa at the cathode with cations causing *n*-doping). The doping at the interfaces, in this case, leads to easier charge injection and enhanced performance (see Chap. 6 for experimental details). It should be noted that some researchers believe that it is simply the build up of ionic space charge that is responsible for enhanced performance in LECs, and not electrochemical doping.[10]

While the methods described above differ, the result is the same: incorporation of ions to stabilize redox defects [solitons and (bi)polarons] on the polymer backbone. In practice, the choice of dopant salt is limited by several factors. First, the salt must go into solution, thus necessitating the use of species with relatively weak ionic binding. For example, NaCl will not readily dissociate in organic solvents, whereas $TBABF_4$ will. Second, the salt must show doping activity. While not completely understood, a variety of salts meeting the solubility criteria have been shown empirically to exhibit effective doping for a wide range of polymers and solvents – *e.g.*, sodium *p*-toluenesulfonate and tetrabutylammonium perchlorate (Chap. 4 and references therein), lithium tetrafloroborate,[8] or $TBABF_4$ (Chap. 6 and references therein).

Table 2.1: Symbols for annotated energy diagram (Fig. 2.6).

symbol	meaning	equivalent
E_{vac}	vacuum energy, equal to 0 eV	
E_g	energy gap between HOMO and LUMO	$= E_{\mathrm{HOMO}} - E_{\mathrm{LUMO}}$
E_{HOMO}	HOMO energy relative to E_{vac}	
E_{LUMO}	LUMO energy relative to E_{vac}	
Φ_{mi}	work function of electrode i	
Φ_{bni}	barrier for electron injection from elec. i into LUMO	$= \Phi_{mi} - E_{\mathrm{LUMO}}$
Φ_{bpi}	barrier for hole injection from elec. i into HOMO	$= E_{\mathrm{HOMO}} - \Phi_{mi}$

2.5 Charge Injection

Unlike the original experiments with PA and PPy where the charge carriers were chemically generated by incorporation of a chemical dopant,[5,6] charge can also be created by direct injection from an electrode interface. In the most common incarnation of this method, a thin film of conducting polymer is sandwiched (see Sec. 3.1) between two metallic electrodes. Lacking any internal dopants, the polymer is in its "intrinsic" state (*i.e.*, it lacks any intrinsic mobile carriers), and can be defined energetically by its HOMO and LUMO energies. The materials – most often metals – chosen as electrodes are selected based on their work function, Φ_m, relative to the polymer energy levels. Typical metals are Au, Ag, Al, and Ca, with Φ_ms ranging from near the usual HOMO energy of conducting polymers ($\sim$5 eV†) to nearer the usual LUMO energy ($\sim$2 eV†). An example energy diagram is shown in Fig. 2.6 where the electron energy increases vertically.

On application of a voltage, V, between the two electrodes, the energy difference between the electrodes is shifted by an additional energy of $-eV$, where e is the elementary

†These energies are always reported as positive numbers, but really refer to electron binding energies. Therefore, they should more appropriately be considered as negative energies relative to the vacuum energy at 0 eV. For example, an electron would need to excited by 2 eV to get from the HOMO level at 5 eV to the LUMO at 3 eV.

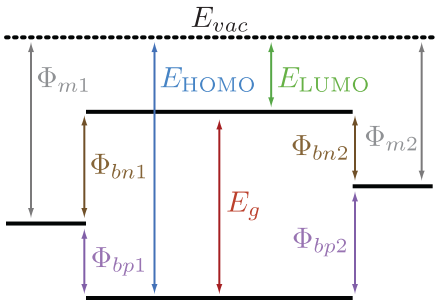

Figure 2.6: Annotated energy diagram for analysis of charge injection into intrinsic polymers using an electrode-polymer-electrode sandwich structure. In this depiction, the vertical axis is electron energy, and the horizontal direction is meant only to indicate the relative placement of the materials. This configuration, known as "flat band", assumes that a voltage is being applied between the electrodes equivalent to the energy difference in their work functions – *i.e.*, $V_{applied} = \frac{1}{e}|\Phi_{m1} - \Phi_{m2}| \equiv V_{bi}$, the "built-in" potential. An example of a device for which this diagram would apply would be a thin film polymer deposited on an evaporated Au bottom electrode (on the left of the diagram) with an evaporated Al top electrode (on the right). The symbols used are described in Table 2.1.

electronic charge and the minus sign accounts for the positive vertical axis indicating *electron* energy. The energy diagram in the case of external bias is shown in Fig. 2.7, parts (a) and (b). Here, the application of a positive (a) and negative (b) voltage to the left electrode relative to the right electrode is evident as a shift in energy of $-eV$.[†] Due to the intrinsic nature of the polymer, there are no mobile charges which can rearrange to partially cancel the resulting electric field within the device. Thus, the shape of the interfacial barrier for charge injection is a simple triangle (Fig. 2.7c), and the electric field within the device can be expressed as

$$\vec{E} = \frac{V}{L}\hat{n}, \tag{2.2}$$

where V is the applied voltage bias, L is the thickness of the polymer layer, and $\hat{n}$ is a unit vector normal to the anode interface. This is in contrast to the familiar Schottky barrier interface of

[†]This voltage V is *in addition* to the "built-in" voltage, $V_{bi} = \frac{1}{e}|\Phi_{m1} - \Phi_{m2}|$, required to attain the flat band configuration.

doped silicon[11] where the interfacial field is non-uniform, and leads to a markedly different voltage response.

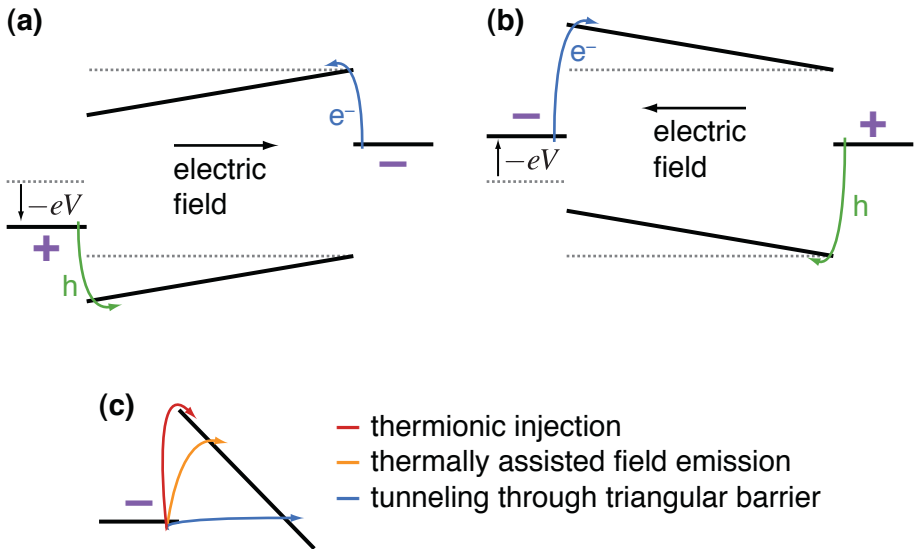

Figure 2.7: Charge injection in sandwiched electrode-polymer-electrode structure into intrinsic polymer. The purple $+$ and $-$ signs indicate which electrode is at a higher voltage/electric potential – recall that the vertical axis is positive *electron* energy. (a) Energy diagram of device biased such that the left electrode is the hole injector (anode or positive electrode) and the right electrode is the electron injector (cathode or negative electrode). (b) Energy diagram with cathode on left, anode on right. In both (a) and (b), the dotted lines indicate the flat band energy levels, and the $-eV$ shift in energy of the left electrode is measured from its flat band level – *i.e.*, $V_{applied} = V + V_{bi}$. Note that the barriers for hole and electron injection (Φ_{bp} and Φ_{bn}, respectively) are unchanged from their values in Fig. 2.6, only shifted. (c) Close up of electron injection in part (b) showing the triangular energy barrier caused by the intrinsic polymer and some of the mechanisms for injection.

By a variety of mechanisms, including thermal excitation, thermally-assisted tunneling, and direct tunneling (Fig. 2.7c), electrons or holes can be injected into – or harvested from – the polymer film. This is simply another way of saying that at sufficient electric field, the polymer can be oxidized or reduced near the electrode interface, causing positive solitons or

(bi)polarons – *i.e.*, oxidation, hole injection – or negative solitons or (bi)polarons – *i.e.*, reduction, electron injection.

While the discussion above is confined to a single clean polymer layer between two metallic electrodes, the same energetic considerations can be applied to multiple layers, blends of materials within the active layer, or even active layers with some form of charge donor/acceptor system (*e.g.*, metallic nanoparticles [Chap. 5], or ionic dopants [Chap. 6]). These, and various other, internal processes can have significant effects on charge transport in the active layer(s) and the resulting device behavior. A sample of such processes are detailed in Fig. 2.8 with some associated effects and uses for each.

Since the discovery of conducting polymers, an extensive research effort has been devoted to characterizing these injection and conduction processes,[†] with the aim of developing both a comprehensive understanding of the fundamental physics and a tool with which to optimize polymer device performance. Two of the chapters to follow deal specifically with this pursuit applied to organic memory devices (Chap. 5) and light-emitting electrochemical cells (Chap. 6).

2.6 Electroluminescence

At the beginning of the 1990s, electroluminescence was first reported in conducting polymers.[13] This process relies on injection of holes and electrons from appropriate electrodes into the HOMO and LUMO energy levels of the polymer, respectively. Here "appropriate" refers to the fact that the work functions of the injecting electrodes must be matched approxi-

[†]For an overview of the various mechanisms with references to recent work on each, see Ref. 12.

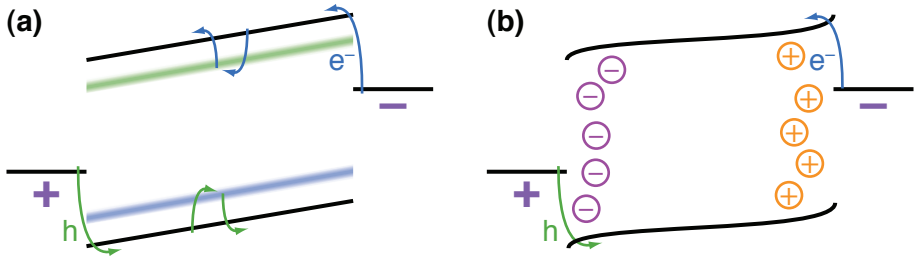

Figure 2.8: A sample of some energetic complications to the simple system of Fig. 2.6. (a) Addition of charge trapping levels within the band gap. Here, electrons and holes are being trapped and are de-trapping from levels near the HOMO and LUMO. Two examples of such a system are the unintentional retention of trapping species from the polymer synthesis (*e.g.*, metal atoms) and the intentional addition of charge traps for memory applications (cf. Chap. 5). (b) Addition of doping species (*i.e.*, ions) within the polymer layer. Under bias, the migration of ions toward the interface causes *n*- or *p*-doping and thus creation of free charges that can affect the internal electric field of the device (cf. Chap. 6). As in Fig. 2.7, the purple + and − indicate which electrode is at a higher voltage/electric potential.

mately with the energy of the level being injected into – *e.g.*, the anode work function should be in the range of HOMO energy. Once injected, the holes and electrons undergo a process known as recombination, where they become Coulombically bound into a neutral species known as an exciton.[†] The exciton can then diffuse around within the polymer (emissive) layer and potentially radiatively decay, releasing a photon in the visible range of wavelengths (due to the 2-3 eV bandgap of most conducting polymers[‡]). The prototypical geometry of such a device, known as an organic LED (OLED) or polymer LED (PLED), is a thin layer of polymer ($\sim$100 nm) deposited between planar electrodes, one of which must be transparent for light to escape (Fig. 2.9). The diode nature of the device is due to the choice of electrode work functions. In "forward" voltage bias, the electrode with work function near the HOMO energy acts

[†]Note that this terminology follows this literature (*e.g.*, Ref. 14) as referring to electron-hole binding, *not* radiative relaxation.

[‡]Recall that $E = h\nu = hc/\lambda$, where h is the Planck constant, c is the speed of light, and ν and λ are the frequency and wavelength of light, respectively. Using the Planck constant in units of eV·s, 2 eV converts to $\lambda = hc/2 = 620$ nm (orange/red), and 3 eV converts to 413 nm (deep blue/violet).

as a good hole injector and vice versa for the electron injecting electrode. However, in "reverse" bias, hole and electrons have much higher energetic barriers to overcome, thus current and light are suppressed, leading to diode behavior.

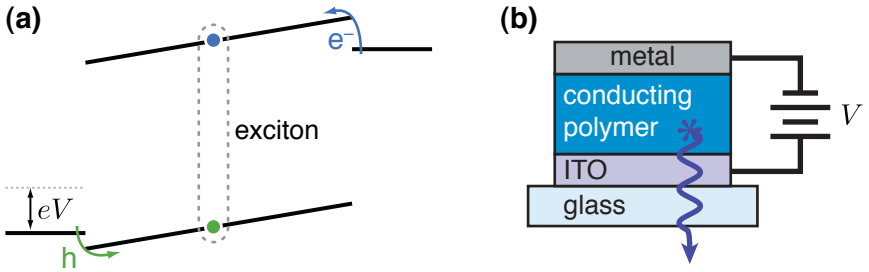

Figure 2.9: Basic organic light-emitting diode structure. (a) Energy diagram of device in "forward" voltage bias (cf. Fig. 2.7). Note that the hole injecting electrode – *e.g.*, indium-tin oxide (ITO) – is nearly aligned with the HOMO, and the electron injecting electrode – *e.g.*, calcium – is nearly aligned with the LUMO. Also note that the exciton is neutral and therefore does not feel the effect of the applied electric field. (b) Physical design of thin film device. Note that one side of the device must be transparent for light output, in this case the transparent indium-tin oxide electrode and glass substrate.

The optimization of this basic OLED structure has comprised a large fraction of conducting polymer research since the initial discovery. At its simplest, the effort is to increase the efficiency of these devices, *i.e.*, to increase the amount of light output for a given electrical current. This specification is parameterized as the "quantum efficiency" (QE) of the device, which is reported in two forms. The *external* QE is a measure of the number of photons measured per electrons injected, a number proportional to the light output (by whatever measurement technique) divided by the device current. The *internal* QE is a measure of the number of photons theoretically created *inside* the device per electrons injected, not taking into account processes such as internal reflection, reabsorption, scattering, etc. In most cases, the external QE – either

on an absolute scale or with arbitrary units – is reported as it is significantly simpler to obtain (see Sec. 3.6).

The process described above is somewhat of an oversimplification. There are a variety of injection processes and a variety of recombination and decay processes that either don't emit "usable" light or don't emit light at all. However, the basic problem lies with the spin statistics of the excitons. Combination of two spin $1/2$ particles – the electron and hole – can yield either a neutral species with spin 0 (the "singlet" exciton) or spin 1 (the "triplet" exciton). The spin 0 singlet state results from the addition of an up spin and a down spin in the same geometric location, where the spin 1 triplet is the addition of two up spins (or two down spins) at slightly different geometric locations. The rapid rate and relatively high efficiency of the radiative decay of singlet excitons to the singlet ground state (fluorescence) provides the bulk of effective light output in most polymer LEDs. The problem is that 75% of the excitons formed in polymer LEDs are triplets, and triplets don't radiatively decay with high enough efficiency into the singlet ground state (phosphorescence, a "forbidden" spin transition).[14,15]

Given this maximum of 25% singlet excitons – and therefore maximum internal QE of 25%[†] – two major research efforts have been undertaken in recent years. One technique is to harvest the triplet excitons in some form of radiative fashion by inclusion of dopant species which can collect the triplet exciton and efficiently phosphoresce (*e.g.*, Ref. 17, and references therein). Another technique is to employ ionic dopants, as described above in Sec. 2.4, to tailor the doping at the interfaces and/or the electric field within the emissive layer. In this way, the

[†]The 25% singlet fraction is based on the naive assumption of equal probabilities for singlet and triplet generation. Recent results (*e.g.*, Ref. 16 and references therein) indicate that the singlet fraction may be significantly greater than 25% in some cases.

efficiency of charge injection can be increased, and thus the QE of the device can be also be increased. This technique forms the basis of light-emitting electrochemical cells (LECs)[9] which are discussed in great detail in Chap. 6 below.

2.7 Photoabsorption and Photovoltaic Effects

The flip side of light emission from decaying excitons (see Sec. 2.6 above) is creation of such excitons by the absorption of incoming light. The mechanism, and the result, are essentially the same as described above for electroluminescence, only in reverse. Incident light with energy equal to the HOMO-LUMO gap energy causes an electron in the HOMO level to be excited into the LUMO, leaving a hole behind.[†] This hole and electron are initially Coulombically bound as a neutral exciton, which can diffuse without regard to the applied (or intrinsic) electric field within the polymer layer. However, if this exciton dissociates, the free electron and hole immediately feel the effect of any electric field present, and can contribute to the current through any circuitry the device is connected to.

This effect is the basis of the field of polymer photovoltaics – specifically solar cells, where light from the sun is converted into energy. The goal in this field is to get the largest amount of current, voltage, or power *out* of the device for a given amount of incident solar flux. The paramterization of polymer solar cells thus focuses on such factors as the maximum current output (the short-circuit current, I_{sc}), the maximum voltage achievable (the open-circuit voltage, V_{oc}), and the light-to-energy efficiency (the reverse of the external QE, described above).

[†]This statement can be said in reverse for a hole being excited from the LUMO to the HOMO. Thus is the duality of holes and electrons.

When the electrodes of a device are short-circuited together (0 V between them), by definition, the energy difference between the electrodes must be zero. Because the alignment of energies at the two polymer-electrode interfaces are fixed,[†] the only way for the polymer layer to adjust to this change is to support shifted bands, as shown in Fig. 2.10a, creating an electric field within the device.[‡] When light is shone on the device and the photogenerated excitons dissociate, free electrons and holes feel this field and contribute to a current, known as the short-circuit current, I_{sc}. This is the maximum sustainable current that can be delivered by the device, limited by such factors as the average distance an exciton diffuses before dissociating, the rate at which free charges recombine into excitons to be potentially re-emitted (fluorescently or phosphorescently) or lost to non-radiative decay, and the incident light flux. This last point is accounted for by using standardized incident light flux. In the case of the research presented below, the AM 1.5 Global spectrum standard[19] is employed. This standard is meant to simulate the average flux of sunlight incident on the 48 contiguous states of the United States of America – *i.e.*, 1000 W/m^2 of solar spectrum light.

As shown in Fig. 2.10b, there is another parameter that can be obtained by this type of current versus voltage analysis: the open-circuit voltage, V_{oc}, *i.e.*, the maximum *voltage* that the device can sustain between electrodes. Specifically, V_{oc} is the voltage that would be measured[§] between the electrodes in the dark. A more appropriate way to measure the effective V_{oc} is to illuminate the device – thus creating excitons and free charges – and determine the voltage that

[†]This is actually a topic of some debate (see, for example, Refs. 12 and 18). However, even given slight variations due to interfacial charge build-up, mirror charges, etc., the energy levels are *close* to fixed, if not actually fixed, at the interfaces.

[‡]Recall that $\vec{E} = -\nabla V$, thus the electric field is determined by the slope of the energy "lines".

[§]The measurement assumes an ideal voltmeter – *i.e.*, infinite input impedance.

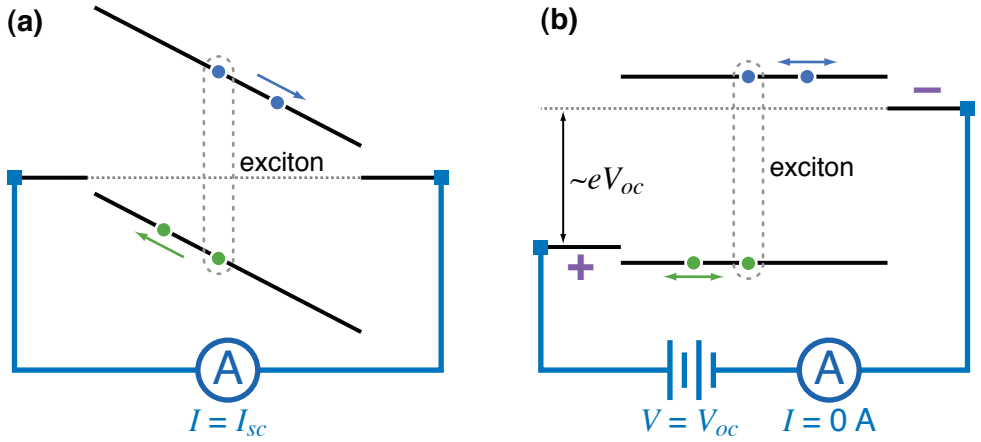

Figure 2.10: Explanation of photovoltaic parameters by experimental example. In both cases, it is assumed that light is being shown on the device causing neutral excitons, which then dissociate into free electrons (●) and holes (●). (a) When the two electrodes are short-circuited together, the matching of Fermi energies causes an internal electric field. The ensuing current of free charges is measured as the short-circuit current, I_{sc}. (b) The effective open-circuit voltage, V_{oc}, is equivalent to the voltage necessary to reduce the photogenerated current to zero – *i.e.*, the voltage necessary to "flatten" the HOMO and LUMO energy bands and remove a preferred direction for free charge to move (cf. Ref. 18). As in Fig. 2.7, the purple + and − indicate which electrode is at a higher voltage/electric potential.

must be applied to cancel any internal electric fields and null the photocurrent by removing a preferred direction for charge motion. While this is not really an open circuit configuration, the voltage measured in this way is equivalent to the true V_{oc} that would be observed during device operation. In the simple illustration of Fig. 2.10, V_{oc} is equal to the built-in potential, V_{bi}, roughly the difference between the electrode work functions.[18] A variety of complications can make V_{oc} not equal to V_{bi}. Most importantly, the exact energy structure of the polymer and/or the electrode(s) is difficult to ascertain.[†] In addition, interfacial effects such as charge build up, dipole layers, or Fermi-level pinning,[12] as well as the exciton kinetics described above, can also effect V_{oc}.

[†]It is notoriously difficult to define a work function for the common electrode material indium-tin oxide (ITO).

The mention above of the various complications in determining I_{sc} and V_{oc} hints at another use of these photovoltaic parameters: to determine the interfacial and/or internal energetic structure of a device. The usefulness of the technique relies on the photoactive nature of conducting polymers, *i.e.*, an intrinsic material can have free charges induced in it by exposure to the proper light source. Indeed, this property of conducting polymers is used below in Chap. 6 to analyse the effects of intentional surface modification by self-assembled monolayers.

2.8 Additional Aspects and Complications

The paragraphs above aim to give a fundamental background into the physics underlying the study and application of conducting polymers. There are, of course, a host of additional topics, not least of which are the subjects of charge trapping within polymer layers, ion diffusion in amorphous polymer films, and polymer electrosynthesis. However, these are specialized topics with basis in the material above. Furthermore, they are discussed in sufficient detail in the chapters to follow. The reader is referred to Chaps. 4 through 6 for more in-depth discussions into these matters.

References

[1] L. Pauling. The nature of the chemical bond. Application of results obtained from the quantum mechanics and from a theory of paramagnetic susceptibility to the structure of molecules. *Journal of the American Chemical Society* **53**, 1367 (1931).

[2] R. S. Mulliken. Spectroscopy, molecular orbitals, and chemical bonding. *Nobel Prize Lecture* (1966).

[3] R. E. Peierls. *Quantum Theory of Solids*. Oxford: Clarendon Press (1955).

[4] C. K. Chiang, J. C. R. Fincher, Y. W. Park, A. J. Heeger, H. Shirakawa, E. J. Louis, S. C. Gau, and A. G. MacDiarmid. Electrical conductivity in doped polyacetylene. *Physical Review Letters* **39**, 1098 (1977).

[5] W. P. Su, J. R. Schrieffer, and A. J. Heeger. Soliton excitations in polyacetylene. *Physical Review B* **22**, 2099 (1980).

[6] R. McNeill, R. Siudak, J. Wardlaw, and D. Weiss. Electronic conduction in polymers. i. the chemical structure of polypyrrole. *Australian Journal of Chemistry* **16**, 1056 (1963).

[7] A. F. Diaz, K. K. Kanazawa, and G. P. Gardini. Electrochemical polymerization of pyrrole. *Journal of the Chemical Society-Chemical Communications* p. 635 (1979).

[8] A. J. Heeger. Nobel lecture: Semiconducting and metallic polymers: The fourth generation of polymeric materials. *Current Applied Physics* **1**, 247 (2001).

[9] Q. Pei, G. Yu, C. Zhang, Y. Yang, and A. J. Heeger. Polymer light-emitting electrochemical cells. *Science* **269**, 1086 (1995).

[10] J. C. deMello, N. Tessler, S. C. Graham, and R. H. Friend. Ionic space-charge effects in polymer light-emitting diodes. *Physical Review B* **57**, 12951 (1998).

[11] S. M. Sze and K. K. Ng. *Physics of Semiconductor Devices*. Wiley-Interscience, 3 edn. (2007).

[12] D. Braun. Electronic injection and conduction processes for polymer devices. *Journal of Polymer Science Part B: Polymer Physics* **41**, 2622 (2003).

[13] J. H. Burroughes, D. D. C. Bradley, A. R. Brown, R. N. Marks, K. Mackay, R. H. Friend, P. L. Burns, and A. B. Holmes. Light-emitting diodes based on conjugated polymers. *Nature* **347**, 539 (1990).

[14] R. H. Friend, R. W. Gymer, A. B. Holmes, J. H. Burroughes, R. N. Marks, C. Taliani, D. D. C. Bradley, D. A. D. Santos, J. L. Bredas, M. Logdlund, and W. R. Salaneck. Electroluminescence in conjugated polymers. *Nature* **397**, 121 (1999).

[15] W. Helfrich and W. G. Schneider. Transients of volume-controlled current and of recombination radiation in anthracene. *Journal of Chemical Physics* **44**, 2902 (1966).

[16] M. Wohlgenannt, K. Tandon, S. Mazumdar, S. Ramasesha, and Z. V. Vardeny. Formation cross-sections of singlet and triplet excitons in π-conjugated polymers. *Nature* **409**, 494 (2001).

[17] X. Yang, D. Neher, D. Hertel, and T. K. Däubler. Highly efficient single-layer polymer electrophosphorescent devices. *Advanced Materials* **16**, 161 (2004).

[18] J. C. Scott, P. J. Brock, J. R. Salem, S. Ramos, G. G. Malliaras, S. A. Carter, and L. Bozano. Charge transport processes in organic light-emitting devices;. *Synthetic Metals* **111-112**, 289 (2000).

[19] ASTM International, Subcommittee G03.09. *G173-03e1 Standard Tables for Reference Solar Spectral Irradiances: Direct Normal and Hemispherical on 37° Tilted Surface*. ASTM International.

Chapter 3

Experimental Techniques

3.1 Solid-State Device Fabrication[†]

Every experiment must begin with something to experiment on, thus we begin with a discussion of device fabrication. A variety of device structures have been developed, but most rely on thin films of conducting polymer sandwiched between, or deposited above, electrodes of some sort. Using this basic architecture, and choosing the right materials, one can make polymer light-emitting diodes (LEDs), transistors, or solar cells (Fig. 3.1). In all of these examples, there are at least three processes required to construct the device on a given substrate: deposition of the bottom electrode(s), deposition of the organic/polymer layer(s), and deposition of the top electrode(s). These processes are discussed in detail below.

Beginning with an appropriate substrate – plastic, glass, silicon, etc. – the first step in fabrication is deposition of the bottom electrode(s). These are often patterned in some way that can produce specific device geometry in conjunction with the top electrode(s). For optically active devices (LEDs, solar cells), the substrate and bottom electrode are generally selected as the transparent interfaces for light to get in or out. In these cases, a common method is to use

[†]Fabrication of conducting polymer devices is a field of research unto itself, and the paragraphs that follow are focused mainly on rough techniques, and not on optimization.

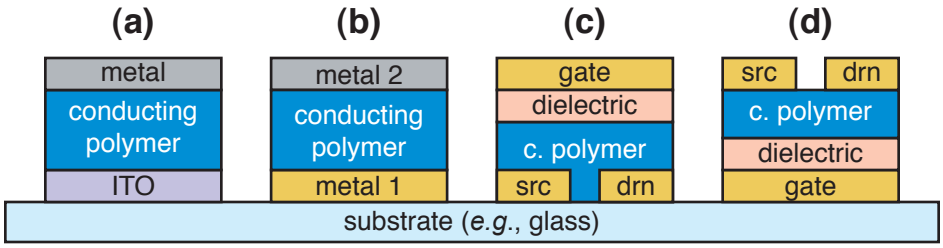

Figure 3.1: Simplified examples of four conducting polymer-based device architectures. (a) Optically active device, *e.g.*, LED or solar cell. Here a glass substrate/ITO combination provides bottom transparency. (b) Non-optical device, *e.g.*, the memory devices of Chap. 5. (c,d) Top- and bottom-gate transistors, respectively.

a glass substrate with patterned indium-tin oxide (ITO) as the bottom electrode. Deposition of ITO can be achieved by many routes, among them photolithograpy, chemical vapor deposition, and sputtering. The ITO substrates used in Chap. 6 were fabricated via sputtering. In this process, a solid disk of ITO ($\gtrsim 100$ cm^3, *i.e.*, palm-sized or larger) is bombarded with high-momentum particles such as atomic ions or noble gas atoms. These particles cause some ITO to be ejected which, due to momentum conservation, follows a known trajectory. The clean glass substrate is fitted with a mask covering the glass everywhere but over the desired electrode location, and is placed in the "line-of-fire" of the ejected ITO. Over time, the ITO landing on the glass forms a continuous layer, and the bottom electrode is formed. The sputtering process is not specific to ITO, and can be used for a large variety of materials – notably more standard electrode materials such as Au, Al, etc. However, the equipment is expensive and requires expertise. For this reason, sputtering is often contracted.[†]

There are, of course, other bottom electrode materials. If the devices is not optically active, as in the case of the memory devices of Chap. 5, metals can be used. In this case, thermal

[†]The ITO sputtering for the research in Chap. 6 was contracted out to a supplier (Thin Film Devices, Inc.).

evaporation under vacuum is the most often employed deposition technique. In this technique, the masked device is placed in a vacuum chamber along with a small sample of the electrode metal, which is placed on or around a resistive heating element (often a tungsten "boat"). The system is brought to a vacuum around 10^{-5} torr, and current is fed through the heating element. The combination of heat and low pressure allows the metal to melt and boil, or simply sublime. Generally, the metal source is placed at the bottom of the vacuum chamber, and the masked devices is placed face-down near the top so that the metal evaporates up toward the device. A deposition meter is also placed near the device so that the rate and thickness of the incoming metal can be observed during deposition. Often, a movable shutter is placed in front of the device so that precise control of thickness can be achieved. Evaporative deposition of this form can be used for both bottom and top electrodes.

Deposition of the polymer layer(s) can also be achieved by many routes: spin casting, drop casting, screen printing, and ink jet printing. All of these techniques rely on the solution processable nature of conducting polymers. The polymer is dissolved in an appropriate solvent (plus any desired additives, such as a second polymer, nanoparticles, etc.), and it is this solution that is used for actual deposition. Once deposited and patterned, the solvent can be evaporated at elevated temperature and/or low pressure, resulting in the thin polymer film. The printing techniques are generally used for high-throughput industrial applications, and are only slight modifications on existing technologies. For this reason, the discussion below will focus mainly on spin casting as it is the method used in Chaps. 5 and 6. This method consists of placing the substrate (with any bottom electrodes already fabricated) with a drop of polymer solution on

it on the axis of rotation of a "spinner".[†] The entire device is spun at high speed – *e.g.*, 2000 rpm for 30 s – and centrifugal force spreads the drop of solution into a very thin flat layer, often hurling a fair volume off entirely. Gross patterning of this layer can then be achieved by wiping away portions of the still-wet film (often with the aid of solvents). The device is then ready for "annealing": solvent evaporation and, in some cases, polymer ordering. Note that drop casting is essentially the same method, except the device is never spun, thus yielding thicker films.

A final note on fabrication is that conducting polymers are often very sensitive to oxidative degradation. For this reason, they must either be stored in an oxygen-free environment, such as a dry box, or encapsulated in some way, such as with an epoxy coating. The devices discussed in Chaps. 5 and 6 were stored and tested in a nitrogen-filled dry box.

3.2 Three Electrode Electrochemistry

Unlike the solid-state devices of Chaps. 5 and 6, conducting polymers can also be utilized and analyzed in solution. This can either be achieved with the polymer dissolved completely in a solvent – *e.g.*, transmission spectroscopy of MEH-PPV dissolved in chlorobenzene – or with a solid polymer film on the surface of an electrode in an "electrochemical cell". This second technique forms the basis of the research presented in Chap. 4 and is elaborated on in detail below.

An electrochemical cell is an electrical circuit containing one electrode undergoing reduction (electrons from the circuit being consumed in a chemical reaction) and one electrode undergoing oxidation (electrons being liberated into the circuit). The electrodes are physically

[†]In practice, the substrate is often held in place using a vacuum chuck.

connected with electronic circuitry and through a "salt bridge", *i.e.*, ions are used as charge carriers within half of the circuit. The basic system is depicted in Fig. 3.2. Under the proper conditions[†] redox reactions occur at the electrodes and current flows in the system. For example, if one electrode is a bar of Cr and the other is bar of Ag, the two "half-reactions" comprising the cell would be written as,

$$\mathrm{Cr}_{(s)} \rightarrow \mathrm{Cr}^{3+}_{(aq)} + 3e, \tag{3.1}$$

and

$$\mathrm{Ag}^{+}_{(aq)} + e \rightarrow \mathrm{Ag}_{(s)}, \tag{3.2}$$

where the two metal rods are immersed in an appropriate salt solution – *e.g.*, $1M$ KNO_3 in water. Each of these reactions requires a certain amount of energy, thus defining a specific energy for the entire electrochemical cell to undergo redox. These energies, known as half-cell potentials, are essentially impossible to determine independent of each other. For this reason, standard electrodes with empirically established half-cell potentials can be used to fix one half of the cell, thus enabling determination of the other half-cell potential and precise control over redox reactions. The most fundamental of these is the standard hydrogen electrode (SHE), which consists of a Pt electrode in a stream of H_2 gas. In this case, the half-cell potential of the reaction at the SHE electrode is defined as 0 V and whatever voltage is measured between the SHE and the other electrode is taken as the half-cell potential for that reaction *vs SHE*. Another common standard is the saturated calomel electrode (SCE), which consists of a Hg electrode surrounded by Hg_2Cl_2 surrounded by water saturated with KCl (known as "calomel"). The

[†]Some combinations of electrodes and electrolytes produce spontaneous currents, others require a voltage or current stress to undergo redox.

half-cell potential for this electrode/reaction is always 0.242 V vs SHE,[1] and can thus be used as a reference. Half-cell potentials for the unknown electrode can be referenced in units of V vs SHE or V vs SCE, where the number should differ by 0.242 V. The SCE electrode is used below as reference in Chap. 4.

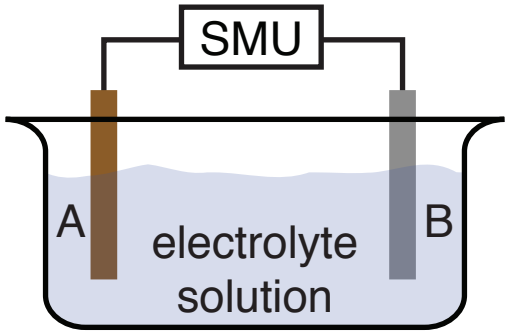

Figure 3.2: Schematic of a simple electrochemical cell. Half of the "circuit" is electronic (through the SMU) and half is electrochemical (through the electrolyte solution). The redox of the two electrodes A and B each contribute to the overall chemical activity, and thus the voltage drops across the cell.

Many electrochemical cells require a fixed voltage to be maintained at one electrode (relative to the reference/standard) for the redox reaction to occur. This is not a trivial task, given the ability of ions in solution to rapidly reorganize to cancel some or all of the applied electric field, much like a liquid dielectric (or conductor). To get around this difficulty, *three* electrode electrochemical cells are employed. The basic methodology of the three electrode cell is shown in Fig. 3.3. In the figure, the negative feedback to the inputs of the the amplifier causes any current necessary to be supplied through the counter electrode to keep the reference electrode at V_{cell} V *below ground*. Since the working electrode is grounded, this is equivalent to keeping the working electrode at V_{cell} V *above* the voltage at the reference electrode. In practice, this circuitry is provided by a dedicated piece of equipment known as a potentiostat.

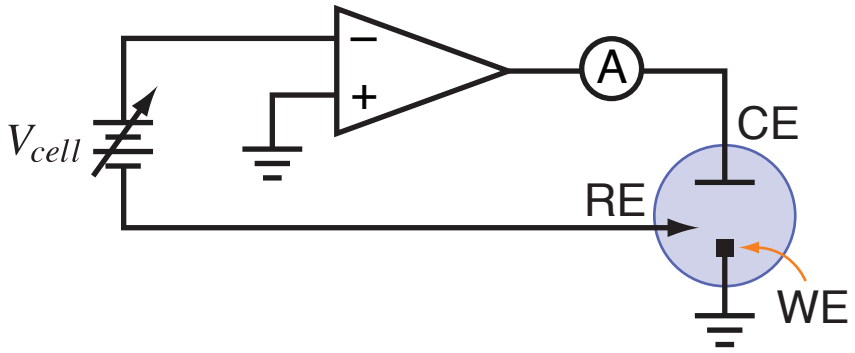

Figure 3.3: Basic circuitry for a three electrode electrochemical circuit. The counter electrode (CE), reference electrode (RE), and working electrode (WE) are immersed in the liquid cell, and the negative feedback circuitry maintains the voltage at the RE at V_{cell} V *below* the voltage at the WE (ground) – *i.e.*, $V_{CE} < V_{RE} < V_{WE}$. Note that this circuit is a gross simplification of the actual circuitry found in a real potentiostat. For the original figure and further discussion on potentiostat design, the reader is referred to Ref. 1.

For the research presented in Chap. 4, the potentiostat controlled three electrode cell consisted of a platinum counter electrode, the SCE reference electrode, and a TiN working electrode for use in a polypyrrole polymerization reaction. This procedure is explained in detail in Refs. 2 and 3, but can be summarized with the equation,

$$2\mathrm{Py} \rightarrow \mathrm{Py}_2 + 2e + 2\mathrm{H}^+, \tag{3.3}$$

or for two polypyrrole chains with n and m repeat units,

$$\mathrm{Py}_n + \mathrm{Py}_m \rightarrow \mathrm{Py}_{n+m} + 2e + 2\mathrm{H}^+. \tag{3.4}$$

In actuality, the reaction takes place in a solution containing doping ions (cf. Sec. 2.4) and some of the oxidation of the polypyrrole is stabilized in the form of (bi)polarons. Thus, the polypyrolle is synthesized in its conductive state. For more details, the reader is referred to Refs. 2 and 3, Sec. 2.4 above, and Chap. 4 below.

As discussed in the other sections of this chapter, the experimental system is ideally configured to be computer controlled and monitored. To this end, the potentiostat used below (an EG&G Princeton Applied Research model 362) was controlled via dual GPIB-connected Hewlett Packard model 3245A universal sources. This enabled computer control of V_{cell} (as shown in Fig. 3.3). The cell current was also monitored over GPIB via a Keithley Instruments model 2000 multimeter (the ammeter of Fig. 3.3). The system was programmed and recorded with a custom-made Igor Pro user interface similar to that described in App. C.

3.3 Current Versus Voltage Analysis

Easily one of the most common experimental techniques in the field of organic electronics – and device electronics in general – is measurement of device current, I or J,[†] as a function of applied voltage, V, resulting in the I-V (or J-V) response. The basic experimental setup is shown in Fig. 3.4, where a specified voltage is applied across the "device under test" (DUT) and the current in the circuit is measured. The simplest imaginable DUT would be an ideal resistor. In this case, the I-V response would obey Ohm's law, $I \propto V$, and a plot of the data on linear I versus V axes would yield a straight line.

The power of I-V analysis becomes apparent, of course, when the nature of the DUT is unknown. If the experimental result shows that $I \propto V$, then it can be said that the device behaves Ohmically. However, real DUTs rarely exhibit such simple behavior. Depending on the internal structure of the device, and its resulting I-V response, the relationship between I and V can exhibit any number of functional forms: power law, exponential, etc. Luckily for

[†] I generally refers to the current, whereas J generally refers to the current density (current/area).

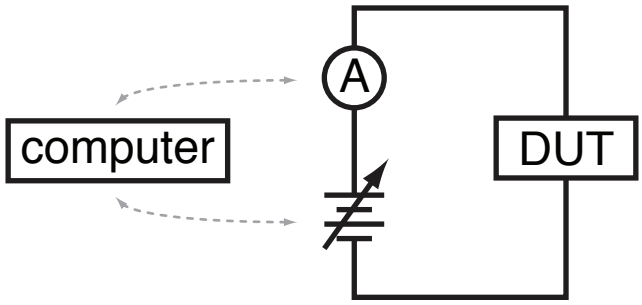

Figure 3.4: Basic circuit for measurement of current versus voltage (*I*-*V*) data acquisition. In general practice, both the voltage source and ammeter are connected to a computer (cf. App. B). Furthermore, they are often contained within the same instrument, *e.g.*, a Keithley 2400 source meter.

the experimentalist, a variety of theoretical models[4,5] have been developed which contain well defined relationships between the current and the voltage. Several of these mechanisms, and their functional dependence are shown in Table 3.1. Briefly, the four models detailed in the table can be explained as follows: diffusion refers to devices where the current is limited by the diffusion of charge within an intrinsic region; space-charge-limited refers to devices where the current is limited by a build up of charge at one or both of the injecting electrodes; Frenkel-Poole emission refers to conduction across a series of deep trap sites within the devices; and Fowler-Nordheim tunneling refers to current limited by the tunneling of charge across a triangular barrier (cf. Fig. 2.7). When the *I*-*V* data appears to fit one of the models functionally over a given range of voltage, then the system proposed by the model is invoked as an appropriate description of the device within that voltage range.

Any combination of analog or digital voltage sources and ammeters can in theory be used for *I*-*V* analysis. However, in practice, computer controlled high precision measurement equipment is employed. Specifically, the data presented in the chapters to follow were obtained

Table 3.1: Some common conduction mechanisms and their associated *I*-*V* functional dependence. Also shown are graphing techniques which should result in the data lying on a straight line if the device obeys the given model. The variable α represents a constant parameter at fixed temperature.

Conduction Mechanism	Functional Dependence	Graphing Technique	Refs.
Diffusion	$I \propto \exp(V)$	$\log(I)$ vs. V	5,6
Space-charge-limited	$I \propto V^2$	$\log(I)$ vs. $\log(V)$	4–6
Frenkel-Poole emission	$I \propto V \exp\left(\alpha\sqrt{V}\right)$	$\log(I/V)$ vs. $\sqrt{V}$	5–7
Fowler-Nordheim tunneling	$I \propto V^2 \exp(-\alpha/V)$	$\log(I/V^2)$ vs. $1/V$	5,8

using a Keithley Instruments model 2400 source meter controlled via a custom-made Igor Pro software interface (cf. App. C). The Keithley 2400 is a GPIB-accessible (cf. App. B) arbitrary current or voltage source that can concurrently measure the voltage, current, resistance, etc. It is thus an ideal tool for computer controlled acquisition of *I*-*V* data. In a typical *I*-*V* experiment, a voltage sweep is specified in the software interface by an initial voltage, a final voltage, the voltage step-size, and the time delay between voltage step and current measurement (the "step-measure delay"). Once programmed, the Keithley 2400 performs the voltage sweep, measuring the current in the circuit at each step, then returns this data to the computer at the end of the sweep. A typical voltage sweep would be from 0 to $+5$ to -5 back to 0 V, with a step size of 0.1 V and step-measure delay of 100 ms. This would be programmed as three sweeps: 0 to $+5$ V, $+5$ to -5 V, and -5 to 0 V. For further details on the specific methods used within this manuscript, the reader is referred to App. C.

3.4 Impedance Spectroscopy[†]

While relatively steady-state measurements such as *I*-*V* analysis are extremely useful, a device's response to ac signals can also be of great use. A common method of profiling this ac response falls under the blanket name of impedance (or immittance[11]) spectroscopy (IS), where the spectrum referred to is the range of ac driving frequencies. The basic experimental technique as used in this manuscript is shown in Fig. 3.5. A driving voltage of the form $V(\omega,t) = V_{dc} + V_{ac}e^{i\omega t}$ is supplied by the voltage source across the DUT and a low-resistance load resistor, R_L, where this resistance must be much less than than the resistance of the DUT. A lock in amplifier phase-synchronized to the voltage source then measures the ac voltage drop, $V_{L,ac}$, across R_L and its phase shift, θ, relative to the source. A multimeter measures the dc signal, $V_{L,dc}$, across R_L concurrently.

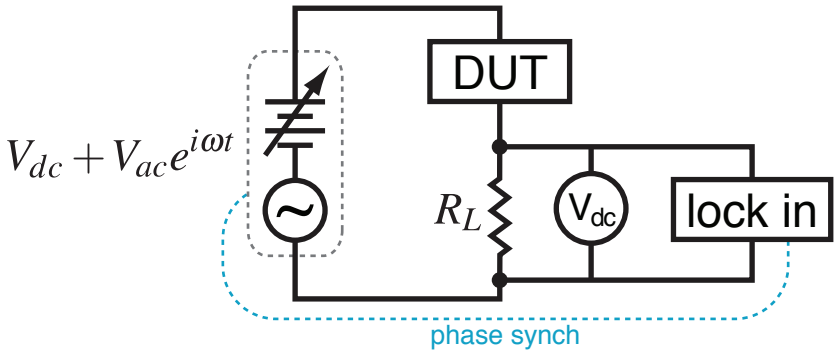

Figure 3.5: Basic circuit for impedance spectroscopy measurements. In general practice, all equipment is connected to a computer (cf. App. B). Furthermore, there exist impedance measurement devices that contain all of the above functionality within a single unit.

[†]A great body of literature is available on this topic, therefore the following discussion is directed at a working understanding of the specific methods used in this manuscript. In particular, the reader is referred to Refs. 9 and 10.

Determination of $V_{L,ac}$ and θ allows for the ac component of the complex current through the circuit to be written as

$$\boldsymbol{I} = \frac{1}{R_L}\left(V_{L,ac}e^{i(\omega t+\theta)}\right). \tag{3.5}$$

Invoking a complex form of Ohm's law, the complex impedance can then be written as,

$$\boldsymbol{Z} = \frac{\boldsymbol{V}}{\boldsymbol{I}} = \frac{V_{ac}e^{i\omega t}R_L}{V_{L,ac}e^{i(\omega t+\theta)}} = Z' - iZ'', \tag{3.6}$$

where Z' and Z'', the real and (negative) imaginary parts of $\boldsymbol{Z}$ respectively, are common variables for the presentation of IS data in the form of a Cole-Cole plot.

An example Cole-Cole plot is shown in Fig. 3.6 for the parallel resistor-capacitor circuit shown in the figure. For this type of circuit,

$$Z' = \frac{1}{R\left(R^{-2}+\omega^2C^2\right)} \tag{3.7}$$

and

$$Z'' = \frac{\omega C}{R^{-2}+\omega^2C^2}. \tag{3.8}$$

Solving Z'' in terms of Z' gives

$$Z'' = \sqrt{Z'}\sqrt{R-Z'}, \tag{3.9}$$

i.e., a semicircle on the Cole-Cole plot with frequency increasing from 0 at the positive Z' intercept to infinity at the origin. Analysis of the geometry of this semicircle shows that the diameter is equal to R, making the maximum value of Z'' equal to $R/2$. Solving Eqns. 3.7 or 3.8 yields $C = 1/\omega R$, so all one needs to determine C is ω at this point. Modifications to the circuit naturally modify the shape of the curve on the Cole-Cole plot.

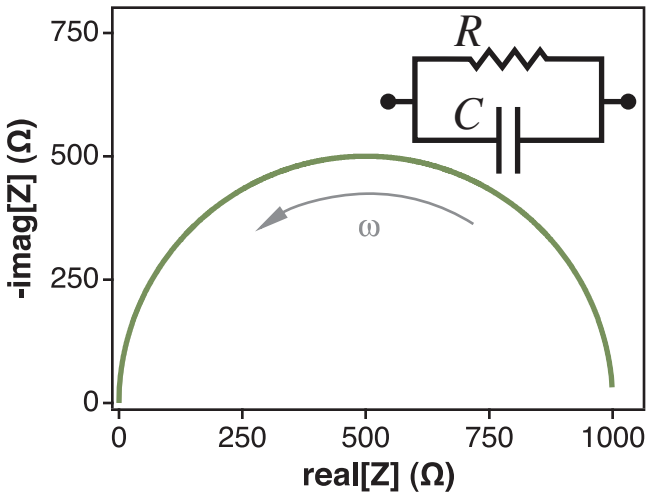

Figure 3.6: Example Cole-Cole plot for the parallel resistor-capacitor circuit shown. In this case, the diameter is equal to R (here, 1 kΩ), making $\max[Z''] = R/2$. Solution of Eqns. 3.7 or 3.8 with this value yields $C = 1/\omega R$ for the ω at this point.

The complex impedance $\boldsymbol{Z}$ is one of many immittance functions that can be derived from IS data.[11] The other two most commonly used immittances are the admittance, $\boldsymbol{Y} = 1/\boldsymbol{Z}$, and the dielectric susceptibility, $\boldsymbol{\chi} \propto -i/\omega\boldsymbol{Z}$.[†] Each immittance has a specific applicability. $\boldsymbol{Z}$ is most useful when analyzing devices of a serial nature. For example, in studying a device that is expected to behave like a serial combination of circuit elements, the impedance of the entire device would simply be the addition of each individual impedance (Fig. 3.7a). The admittance, $\boldsymbol{Y}$, and susceptibility, $\boldsymbol{\chi}$, are both useful in cases of parallel nature: $\boldsymbol{Y}$ for analysis of equivalent circuit behavior and $\boldsymbol{\chi}$ for analysis of dielectric polarization behavior. For example, the admittance of a parallel combination of circuit elements is simply the addition of the inverse impedance of each (Fig. 3.7b).

[†]This $\boldsymbol{\chi}$ is derived for the case of either zero inductance in the device, or the complex capacitance taking account of both capacitive *and* inductive effects.

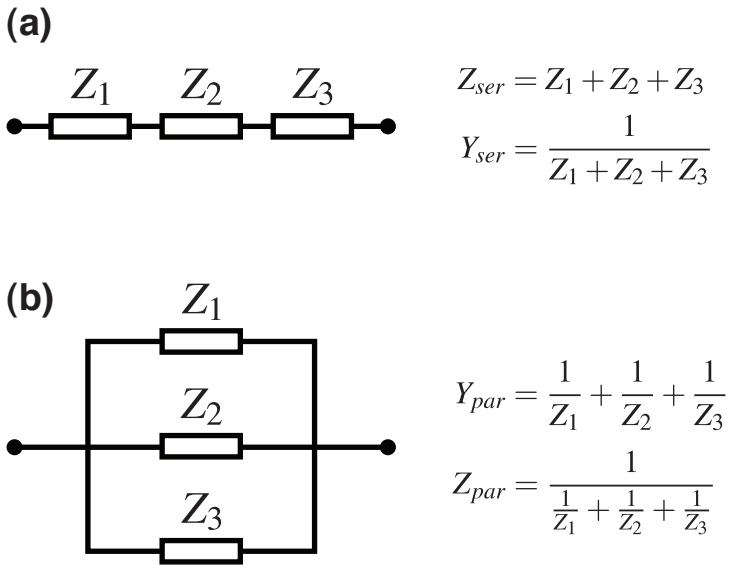

Figure 3.7: Examples of applicability of the complex impedance, $\boldsymbol{Z}$, and complex admittance, $\boldsymbol{Y}$. (a) $\boldsymbol{Z}$ and $\boldsymbol{Y}$ of circuit elements connected in series. (b) $\boldsymbol{Z}$ and $\boldsymbol{Y}$ of circuit elements connected in parallel.

The immittance used in this manuscript (Chap. 5) is the admittance, $\boldsymbol{Y}$. If $\boldsymbol{Y}$ is expressed in terms of real and imaginary parts,

$$\boldsymbol{Y} = G(\omega) + i\omega C(\omega), \tag{3.10}$$

the real part, $G(\omega)$, is the frequency dependent conductance (inverse of resistance), and the imaginary part, $\omega C(\omega)$, gives the frequency dependent capacitance of the device. Note that this formulation assumes that there is either no inductive reactance of the device or that any inductive effects (assumed to be small over the frequencies used and device architectures tested) is taken account of by the frequency dependence of $C(\omega)$. Due to the parallel nature of the admittance, $G(\omega)$ and $C(\omega)$ correspond to a parallel resistor-capacitor ("*RC*") circuit (Fig. 3.8).

For thin film polymer devices in general, and the organic memory devices of Chap. 5 in particular, the admittance and the equivalent circuit of Fig. 3.8 are directly applicable. The

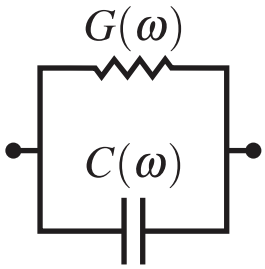

$$\boldsymbol{Y} = G(\omega) + i\omega C(\omega)$$

$$\boldsymbol{Z} = \frac{1}{G + i\omega C} = \frac{1}{G^2 + \omega^2 C^2}\,(G - i\omega C)$$

Figure 3.8: Equivalent *RC* circuit for admittance analysis. Note the simplicity of $\boldsymbol{Y}$ compared to $\boldsymbol{Z}$.

frequency dependent conductance, $G(\omega)$, accounts for purely resistive conduction through the semiconducting film, and for modifications to this "dc" behavior due to the film's internal structure. The frequency dependent capacitance, $C(\omega)$, then accounts for various aspects of "ac" behavior: charge build up, trapping, changes in effective device area, etc. Over-simplifying, $G(\omega)$ elucidates the dynamics of mobile charges, while $C(\omega)$ elucidates the dynamics of trapped and/or stored charges – *i.e.*, their ability to follow a rapidly changing electric field. Clearly, a detailed understanding of where charge is and how it can move within a device is a necessity for fundamental understanding.

In practice, there are various ways of setting up an IS measurement. The simplest is to use a dedicated impedance measurement unit, such as an Agilent Technologies model 4395A combination analyzer. For the measurements detailed below (and depicted in Fig. 3.5), the various functions of the measurement were performed by separate pieces of equipment. Specifically, a WaveTek model 650 universal voltage source was used to generate the dc-shifted driving signal $V(\omega,t)$ over the frequency range 100 Hz to 100 kHz. The physical connection to the DUT and load resistor (the horizontal lines linking the left and right halves of the circuit in Fig. 3.5) consisted of braided coaxial cables to eliminate the pickup of stray high frequency

signals.[†] A Keithley Instruments model 2010 multimeter and Stanford Research Systems model SR830 lock in amplifier were connected in parallel across a high-precision 5 Ω load resistor. The lock in was connected in ac-isolation mode – *i.e.*, the input was passed through a large internal capacitor to separate out the ac component. The measurement system was controlled via the custom-made Igor Pro software interface MultiSweep, described in detail in App. C.

3.5 Current or Voltage Versus Time Analysis

Often the internal structure of a devices can be dynamic. An example of this situation would be the light-emitting electrochemical devices (LECs) of Chap. 6. Here, mobile ions within the polymer film migrate with the applied electric field, and change the internal energetic structure of the device. In cases such as these, the time dependence of the *I-V* response is useful to determine. One method for obtaining this dependence is to profile either the current through the device (at fixed voltage bias) or the voltage drop across the device (at fixed driving current) versus time, yielding *I-T* or *V-T* data, respectively. With this data, characteristic time scales of various internal processes – *e.g.*, ion motion or space-charge build up – can be ascertained. Furthermore, the change in current or voltage with time can show whether a device exhibiting hysteresis has been fully "formed". The time scales used in experiments such as these can range from the very fast (femtoseconds) to the very slow (hours). In the case of the measurements of Chap. 6, the time scale was on the order of minutes.

[†]The closer the DUT is to the measurement apparatus, the better. For this reason, many analyzer units have special attachments that connect the DUT directly to their front panel. However, as all of the devices tested below required an inert atmosphere, the braided coaxial cables were used to test devices within a nitrogen filled glove box.

In general, the measurement apparatus is identical to that shown in Fig. 3.4 (or with a voltmeter and current source), but the computer requests measurement at specific time intervals rather than after sweeps. Electroluminescence measurement can also be conducted concurrently to yield the quantum or power efficiency as a function of time (cf. Sec. 3.6).

3.6 Electroluminescence Analysis

As noted above in Sec. 2.6, much of the study and many of the applications of conducting polymers have been based on their electroluminescent properties. The parameterization of light emission can take a variety of forms: among them spectral analysis (intensity versus wavelength); photoemission, where the light emission is stimulated by an excitation lightsource; and study of overall luminance (total light flux measured as a conversion efficiency or simple brightness). Since only the last of these was employed in this manuscript, the following discussion will focus on determination of luminance and efficiency quantification.

While all polymer electroluminescence exhibits an emission spectrum linked to the energy gap between the HOMO and LUMO levels, it is often of great use to measure the overall light output regardless of wavelength. Generally speaking, the emission spectrum of a given polymer has its highest intensity at a wavelength equivalent to the band gap of the polymer (cf. footnote on pg. 24), with intensity decreasing at higher and lower wavelengths toward zero emission. Detection of this total light output is generally achieved with the aid of a silicon photodiode attached to an ammeter, yielding the "photocurrent" (Fig. 3.9). Calibration with a known light source can then give a conversion factor which enables the photocurrent to be converted to a light intensity.

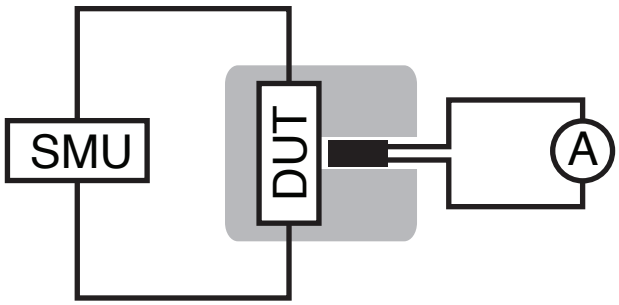

Figure 3.9: Schematic of apparatus for electroluminescence data acquisition. This is essentially the same circuitry as that shown in Fig. 3.4, with the added EL measurement. The gray square represents a dark enclosure, and the small black rectangle represents the silicon photodiode.

In addition to simple integrated intensity, it is also of important to quantify the efficiency of light emission, *i.e.*, how much current is required for a given brightness. The two fundamental efficiencies used in the study of polymer electroluminescence are the quantum efficiency (QE) and power efficiency (PE). As described in Sec. 2.6, there are two flavors of QE: internal and external, where internal is the theoretical conversion efficiency of injected charge into photons, and external is the effective conversion efficiency *outside* a real device. For the remainder of the discussion, emphasis will be placed on the external QE. Fundamentally, the QE is the number of photons emitted divided by the number of electrons injected. Experimentally, one does not measure either of these numbers directly. Instead the light emission is usually detected by a silicon photodiode, yielding a "photocurrent" proportional to the light flux entering the diode. Calibration of the photodiode to a known light source determines this proportionality constant relating photocurrent to actual light flux – *i.e.*, emitted power versus photocurrent. Similarly, the number of electrons injected can be derived from the device current. In this way,

the external QE is calculated as

$$\mathrm{QE} = \frac{N_\gamma}{N_e} = \frac{I_\gamma (X/E_\gamma)}{I_{dvc}/e} = \frac{I_\gamma}{I_{dvc}} \frac{X}{E_\gamma/e}, \tag{3.11}$$

where I_γ is the photocurrent, I_{dvc} is the device current, X is the photodiode current-to-emitted power conversion factor in Watts per Ampere, and E_γ is the average photon energy of the emitted light in J (as determined by spectral analysis), making E_γ/e the average photon energy in eV.

This type of measurement is very often done concurrently with *I-V*, *V-T*, or *I-T* data acquisition. For example, Fig. 6.3 on page 90 shows QE data as a function of time during constant current stressing – *i.e.*, during *V-T* acquisition. Another example is Fig. 6.4 on page 92, where electroluminescence data were obtained during *I-V* sweeping. In this case, the luminance data are presented in units of candelas (cd) per m^2, instead of as a QE.

For the data presented in Chap. 6, the experimental apparatus depicted schematically in Fig. 3.9 was used. In this setup, the DUT is placed in a dark enclosure – specifically, a custom-cut block of black Delrin plastic – and a silicon photodiode is inserted through an opening in the block and pressed against the emissive region. Note that for the devices reported in this manuscript, the light emission is through an ITO electrode on a glass substrate, so pressing the photodetector against the glass does not pose a risk to the thin film itself. The DUT is stimulated (and monitored) by a source meter unit (SMU) – *e.g.*, a Keithley Instruments model 2400 – and the subsequent electroluminescence is detected as a current through the photodiode. For the measurements in Chap. 6, a Keithley Instruments model 485 picoammeter was used to monitor this photocurrent. As described above in Sec. 3.3 and in Apps. B and C, the measurement can be completely computer controlled via GPIB.

3.7 Photovoltaic Analysis

In contrast to electroluminescence, where light is generated by the radiative decay of excited charges, optically active materials such as conducting polymers can also undergo the reverse process: creation of free excited charges by incident light. As discussed above in Sec. 2.7, there are two fundamental parameters that can be measured to characterize photovoltaic response: the short-circuit current, I_{sc}, and the open-circuit voltage, V_{oc}. Fig. 3.10 (duplicate of Fig. 2.10 for convenience) explains these two parameters experimentally.

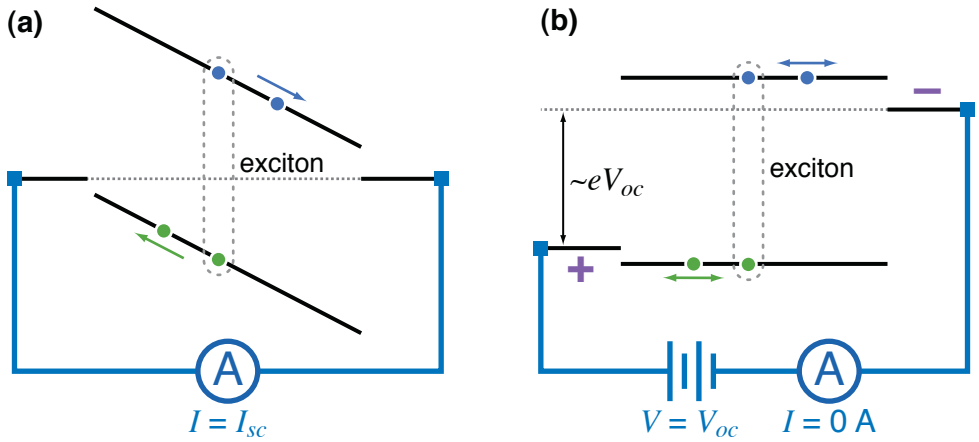

Figure 3.10: Explanation of photovoltaic parameters by experimental example. In both cases, it is assumed that light is being shown on the device causing neutral excitons, which then dissociate into free electrons (●) and holes (●). (a) When the two electrodes are short-circuited together, the matching of Fermi energies causes an internal electric field. The ensuing current of free charges is measured as the short-circuit current, I_{sc}. (b) The effective open-circuit voltage, V_{oc}, is equivalent to the voltage necessary to reduce the photogenerated current to zero – *i.e.*, the voltage necessary to "flatten" the HOMO and LUMO energy bands and remove a preferred direction for free charge to move (cf. Ref. 12). As in Fig. 2.7, the purple + and − indicate which electrode is at a higher voltage/electric potential.

The similarity to electroluminescence measurement extends to the apparatus as well. Fig. 3.11 shows the setup used for the data presented in this manuscript. Here, the photodiode

used to detect light emission is replaced with a light source. The measurement of I_{sc} and V_{oc} is most often performed using an I-V sweep. A sample data set is shown in Fig. 3.12. In the figure, a voltage sweep from -1 to $+1$ V is performed, immediately yielding I_{sc} as the current at zero volts and V_{oc} as the voltage at zero current. The figure also depicts the calculation of the maximum theoretical power deliverable by the device, $P_{max} = |I_{sc} \times V_{oc}|$, as well as the maximum effective deliverable power, $P_{eff} = \max[\,|I(V) \times V|\,]$. The ratio of these two numbers is often reported as the fill factor, FF:

$$\mathrm{FF} = \frac{P_{eff}}{P_{max}} = \frac{|I_{sc} \times V_{oc}|}{\max[\,|I(V) \times V|\,]}. \tag{3.12}$$

The FF gives a succinct expression of a given device's ability to perform optimally: the higher the fill factor, the closer to maximum theoretical power output of the device, regardless of the actual value of that power.

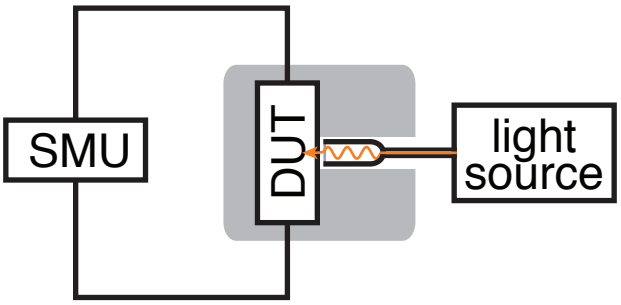

Figure 3.11: Schematic of apparatus for photovoltaic data acquisition. This is essentially the same circuitry as that shown in Figs. 3.4 and 3.9, with the light source added. Again, the gray square represents a dark enclosure.

The specific equipment used for the data presented below in Chap. 6 was similar to the setup described in Sec. 3.6, except for the replacement of the photodiode with a light source. The light source employed here was an Oriel solar spectrum simulator based on a 150 W xenon

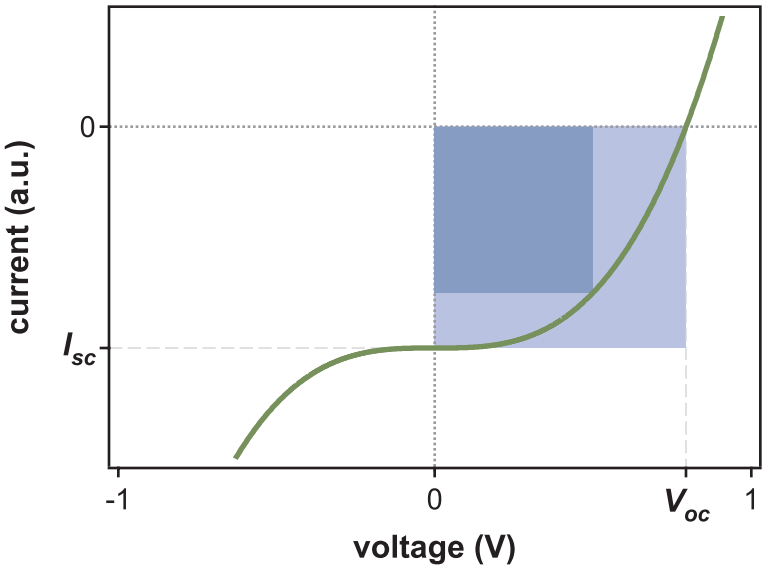

Figure 3.12: Sample current versus voltage sweep showing acquisition of the photovoltaic parameters I_{sc} and V_{oc}. The maximum theoretical power output is shown as the area of light blue square and the maximum effective power output is the area of dark blue square. The fill factor is then the area of the dark blue square divided by the area of the light blue square. Note that the shape of this curve – and thus the fill factor – is dependent on the incident light flux. For this reason, the standard 1000 W/m^2 AM 1.5 flux (Ref. 13) is employed.

arc lamp. The collimated light was guided toward the device by a liquid light guide, enabled testing within a nitrogen glove box, and delivering 1000 W/m^2 of simulated solar flux.[†] As above, the DUT and (light guided) light source were enclosed in a block of black Delrin plastic to prevent stray light from entering the system. Data was acquired in the form of *I*-*V* sweeps, and I_{sc}, V_{oc}, and the FF were calculated from the data using the analytical tools within the Igor Pro software package.

[†]This is based on the AM 1.5 Global spectrum (Ref. 13).

References

[1] A. J. Bard and L. R. Faulkner. *Electrochemical Methods*. John Wiley & Sons, New York (1980).

[2] A. F. Diaz, K. K. Kanazawa, and G. P. Gardini. Electrochemical polymerization of pyrrole. *Journal of the Chemical Society-Chemical Communications* p. 635 (1979).

[3] A. F. Diaz and B. Hall. Mechanical-properties of electrochemically prepared polypyrrole films. *IBM Journal of Research and Development* **27**, 342 (1983).

[4] M. A. Lampert and P. Mark. *Current Injection in Solids*. Academic Press, New York (1970).

[5] D. Braun. Electronic injection and conduction processes for polymer devices. *Journal of Polymer Science Part B: Polymer Physics* **41**, 2622 (2003).

[6] S. M. Sze and K. K. Ng. *Physics of Semiconductor Devices*. Wiley-Interscience, 3 edn. (2007).

[7] J. Frenkel. On pre-breakdown phenomena in insulators and electronic semi-conductors. *Physical Review* **54**, 647 (1938).

[8] E. Ettedgui, H. Razafitrimo, Y. Gao, and B. R. Hsieh. Band bending modified tunneling at metal/conjugated polymer interfaces. *Applied Physics Letters* **67**, 2705 (1995).

[9] E. H. Nicollian and J. R. Brews. *MOS (Metal Oxide Semiconductor) Physics and Technology*. Wiley-Interscience, New York (1982).

[10] A. K. Jonscher. Dielectric relaxation in solids. *Journal of Physics D* **32**, R57 (1999).

[11] J. R. MacDonald, ed. *Impedance Spectroscopy: Emphasizing Solid Materials and Systems*. Wiley-Interscience, New York (1987).

[12] J. C. Scott, P. J. Brock, J. R. Salem, S. Ramos, G. G. Malliaras, S. A. Carter, and L. Bozano. Charge transport processes in organic light-emitting devices;. *Synthetic Metals* **111-112**, 289 (2000).

[13] ASTM International, Subcommittee G03.09. *G173-03e1 Standard Tables for Reference Solar Spectral Irradiances: Direct Normal and Hemispherical on 37° Tilted Surface*. ASTM International.

Chapter 4

Electrosynthetically Patterned Conducting Polymer Films for Investigation of Neural Signaling[†]

Abstract

The ion-mediated conduction and versatility of device fabrication of conducting polymers provide a route to the study of neural signaling. Patterned junctions of conducting polypyrrole have been electropolymerized on commercially available microelectrode arrays, with typical dimensions 200 μm between electrodes, each electrode being 30 μm in diameter. Tetrabutylammonium perchlorate or sodium *p*-toluenesulfonate were used as electrolyte/counterion in the organic solvent. Individual polypyrrole junctions, when synthesized and connected in a three-electrode configuration, exhibit current-switching behavior analogous to neural weighting. Junctions copolymerized with thiophene exhibit current rectification and the nonlinear current-voltage behavior requisite for complex neural systems (*i.e.*, the activation function).

[†]Reprinted with permission from: D. T. Simon and S. A. Carter, *Journal of Chemical Physics* **124**, 204709 (2006).

[doi: 10.1063/1.2200348]

4.1 Introduction

The tunable conductivity and ease of synthesis of conducting polymer films make them ideal for the development of structures exhibiting "neural" dynamics. Like biological neurons, conduction within these films is mediated by ions. Polymers depend on the proximity of counterions to the π-conjugated backbone to stabilize the charge carriers (solitons or polarons),[1] while biological neurons depend on the influx and efflux of ions to produce their electronic signals. Controlling the flow of counterions into and out of these polymer films determines the overall conductivity in a way analogous to weighting of algorithmic neurons (*e.g.*, perceptrons[2,3]). Furthermore, the unique current versus voltage characteristics of certain blends of conducting polymers provide the nonlinear output versus input requisite for the more complicated algorithmic networks which mirror our own biological system.[4] These junctions thus provide an experimental platform which lies between conventional semiconductor-based neural computing, based on purely electronic conduction, and our own biological neural network, which is based on ionic and chemical signal conduction. Extended networks of such junctions could then elucidate an understanding of emergent dynamics in neural processing that would be unattainable in a purely electronic system.

Recent attention has been paid to the use of polypyrrole (PPy) and polythiophene (PThio) for these purposes.[5,6] These conducting polymers can be synthesized electrochemically *in situ* in their conducting state,[7] and thus provide an accessible route to the fabrication of extended networks. Microelectrode arrays (MEAs) have also recently been employed as the working electrode(s) in the synthesis and characterization of conducting polymer films.[8,9]

These devices, developed for analysis of brain slices and cultured neural networks *in vitro*, have individually addressable electrodes embedded in an insulating substrate and are thus also ideal for use in micro-scale electrochemistry. Typical dimensions are $\sim$500 μm^2 electrodes spaced $\sim$200 μm apart. The advantage of using these arrays is that polymer electronics can be patterned by selective electropolymerization above individually addressable electrodes. Multiple junctions could then be synthesized in a "connect-the-dots" fashion, yielding patterened conducting polymer networks.

To date, all research into such neural polymer systems have either been done on a macroscopic scale ($\sim$10 cm) without the use of a potentiostat,[6] employed potentially over oxidizing voltages in the electrosynthesis or "weighting" stages,[10] or used polymers synthesized *ex situ*.[5] Even previous work involving PPy on MEAs (Ref. 8) relied on extended interdigitated electrodes, not today's standard MEA geometry.

In this article, we report on the electrical dynamics of two- and three-electrode junctions electropolymerized on a commercially available MEA. In the three-electrode case, the PPy junctions each have an input, output, and control electrode, and we investigate the response of the output to voltages applied at the control electrode, *i.e.*, neural weighting of signals. In the two-electrode case, the PPy/Thio blend junctions consist solely of input and ouput, and we investigate the nonlinear current versus voltage behavior required for complex neural networks (*i.e.*, the activation, or transfer, function relating the summed inputs to the output).

4.2 Experiment

4.2.1 Materials and Apparatus

Pyrrole monomer, thiophene monomer, sodium *p*-toluenesulfonate (NaTS), and tetrabutylammonium perchlorate ($TBAClO_4$) were used as received from Sigma-Aldrich. Anhydrous acetonitrile (Alfa Aesar) was also used as received. All solutions were prepared in a nitrogen dry box and stored in the dark at 2 °C under nitrogen. The MultiChannelSystems MEA (200μm/30μm-TiN/SiN model) was sonicated for 2 min in de-ionized water and then rinsed repeatedly with de-ionized water and ethanol before each use.

The electrochemical cell used for electropolymerization and three-electrode analysis consisted of the TiN electrodes of the MEA as working electrode(s), a 0.5 mm diameter platinum wire (Aldrich) as counter electrode, and a saturated calomel electrode (SCE) (Accumet) as reference (Fig. 4.1). The reference electrode was inserted into the solution using a 3 ml luggin capillary. All experiments were carried out in air. The cell was controlled via an EG&G Princeton Applied Research 362 potentiostat with dual Hewlett Packard 3245A universal sources. Data was collected on a Keithley 2000 digital multimeter, and the system was imaged during electrosynthesis using a QImaging QCapture charge-couple device (CCD) camera mounted on a Technical Instruments K2S-BIO confocal microscope (on a Nikon upright microscope base).

The solutions used for the two-electrode anaylsis consisted of 0.2M $TBAClO_4$ in acetonitrile with: 0.5M pyrrole ("1:0" solution), 0.25M pyrrole with 0.25M thiophene ("1:1" solution), and 0.167M pyrrole with 0.333M thiophene ("1:2" solution).

4.2.2 Electropolymerization

For the three-electrode devices, PPy was electropolymerized into its conducting state using a solution of 0.5*M* pyrrole monomer and 0.2*M* counterion salt (NaTS or $TBAClO_4$) in acetonitrile. Once added to the well on the MEA (Fig. 4.1), the solution was capped to prevent evaporation. Following the work of Diaz *et al.*,[7] a voltage of 0.8 V vs SCE was applied until the desired area of PPy was formed ($\sim$30–60 min for $\sim$0.2 cm^2). Polymerization was carried out on three adjacent MEA electrodes, labeled I, O, and C in this article for input, output, and control. Voltage was supplied to all three electrodes until just before the polymer films above each electrode were large enough to make electrical contact with the adjacent films. At this point, the outer two electrodes (I and O) were disconnected from the voltage supply, leaving only the central electrode (C) as part of the electrochemical circuit. Current was supplied through the central electrode until its polymer film made electrical contact with the outer two films (Fig. 4.2). The current versus time plot shows that the three electrodes form a contiguous conducting film (Fig. 4.3). The steady increase in current in Fig. 4.3 is indicative of the increase in surface area of the PPy films: as more surface area is created, more sites are made available to add monomer units. The two-electrode PPy/Thio blend devices were electropolymerized in a similar fashion using a solution of pyrrole and thiophene in 0.2*M* $TBAClO_4$ acetonitrile (1:0, 1:1, or 1:2, as described above). In this case, instead of completing the polymerization using the C electrode, the O electrode was used to complete the polymer film in the direction of the I electrode.

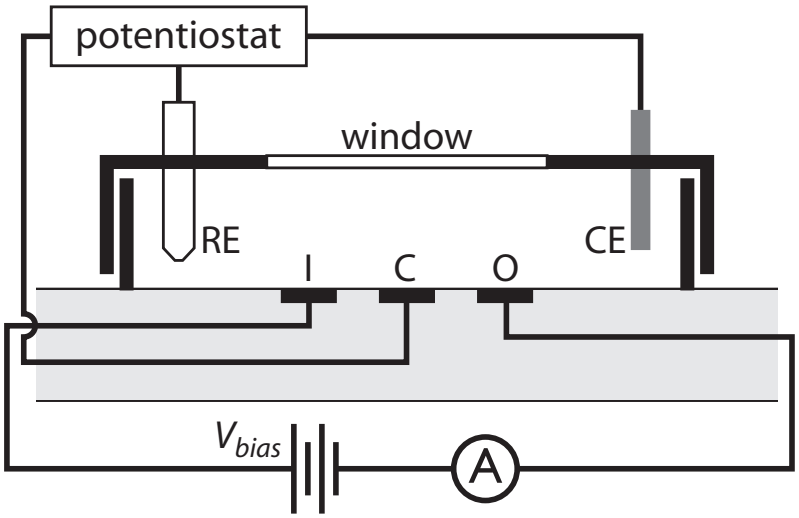

Figure 4.1: The two circuits used in three-electrode analysis showing input (I), output (O), and control (C) MEA electrodes, Pt wire counter electrode (CE), and SCE reference electrode (RE). Only the control electrode is part of the three-terminal potentiostat circuit during the analysis. During polymerization, I and O are connected to C as the composite working electrode.

4.2.3 Device Analysis

The three-electrode analysis was performed by "ionic gating" of the polymer film via voltages applied to the C electode. The input-output circuit and control circuit are shown in Fig. 4.1. A constant voltage, V_{bias}, was supplied across the I-O junction and the I-O current, I_{bias}, was recorded. Potentiostat-supplied voltage pulses (versus SCE), V_c, were then supplied through the control electrode to modulate I_{bias}. Junction rectification analysis was performed using the two-electrode junction with single input and output. An increasing ramp voltage (Fig. 4.8 inset) was applied between the two electrodes (*i.e.*, through the polymer bulk), and the current was measured as a function of the bias voltage. To prevent continued polymerization during analysis, the electrochemical cell was rinsed and refilled with a solution containing only the counterion (NaTS or $TBAClO_4$) in acetonitrile.

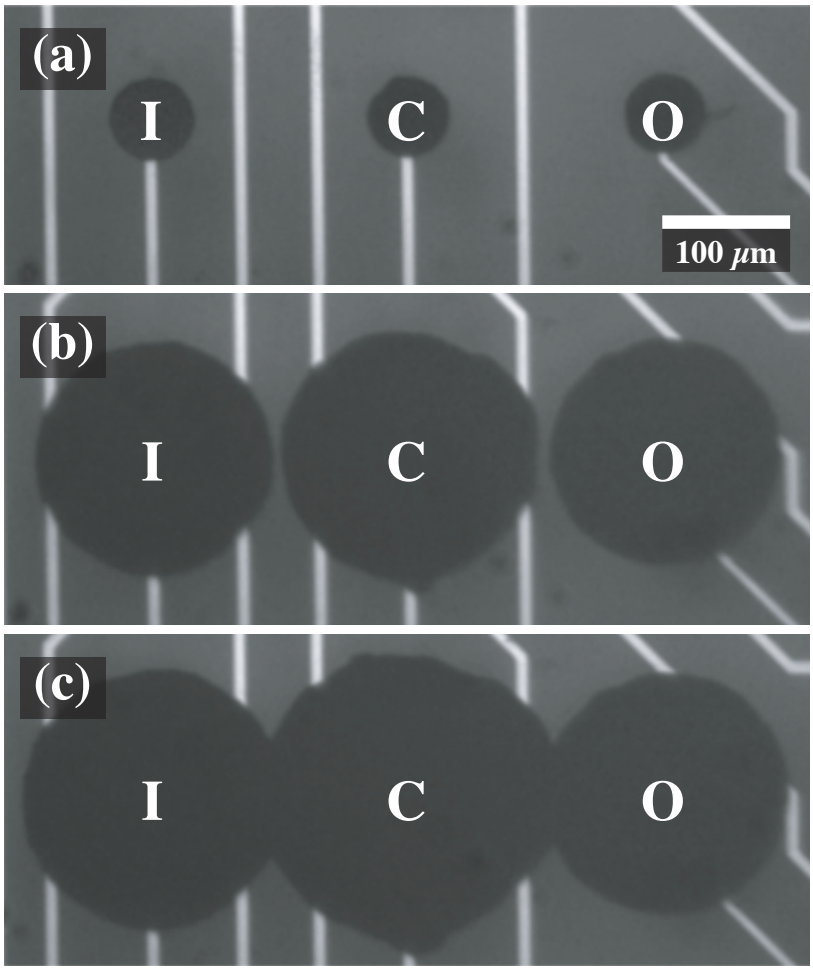

Figure 4.2: Polymerization above three MEA electrodes at three times (where I, O, and C stand for input, output, and control): (a) at 29 min with all three elctrodes connected as the working electrode; (b) at 73 min, when the I and O electrodes have been disconnected from the voltage supply; and (c) at 80 min, after the C film has made electrical contact with the I and O films.

4.3 Results and Discussion

4.3.1 Three-Electrode Ionic Gating Analysis

The results of a typical three-electrode experiment are shown in Fig. 4.4, *i.e.*, the conductivity of the input-output channel can be quasipermanently modulated (weighted) by V_c.

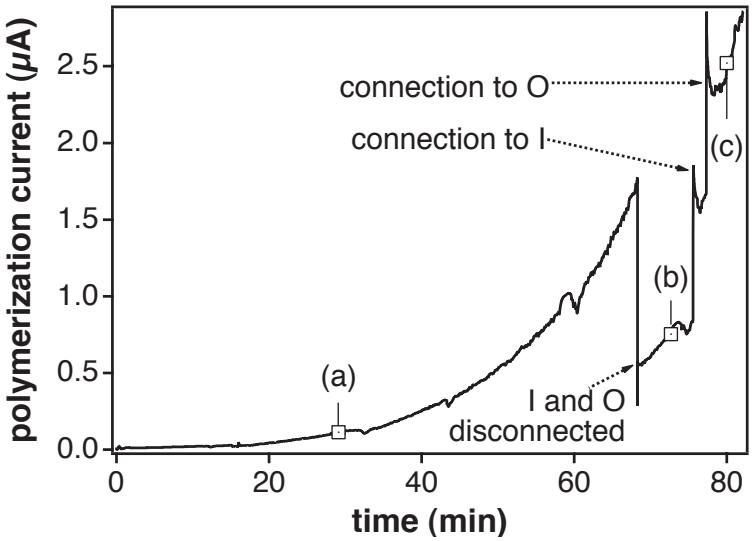

Figure 4.3: Cell current versus time plot associated with the polymerization of Fig. 4.2. The I and O electrodes are disconnected at 68 min, making the C the only working electrode. At 75 min, the C film makes electrical contact with the I film, and then at 77 min, with the O film. The tags labeled a, b, and c, correspond to the images of Fig. 4.2.

This behavior is explained by means of the polaron/bipolaron picture of conduction.[1,11] When $V_c > 0$ (vs SCE), PPy is oxidized and negative counterions (TS^- or ClO_4^-) are attracted toward the film above the C electrode. PPy is known to be in its conducting state when oxidized,[7] *i.e.*, positive (bi)polarons are the charge carriers. When negative counterions are brought into proximity with the π-conjugated backbone of the polymer, positive (bi)polarons can readily be stabilized (charge neutralized) over large interchain distances. In this manner, the conductivity of the overall film increases as hopping sites are made available. Likewise, for $V_c < 0$ (vs SCE), PPy is reduced and the negative counterions requisite for enhanced conduction are swept away from the polymer film, thus decreasing the conductivity.

The overall decrease in I_{bias} with time ($\tau_{global} \approx 45$ min) is due to the exposure of the system to oxygen trapped under the cell cap (Fig. 4.1) and the evaporation of acetonitrile

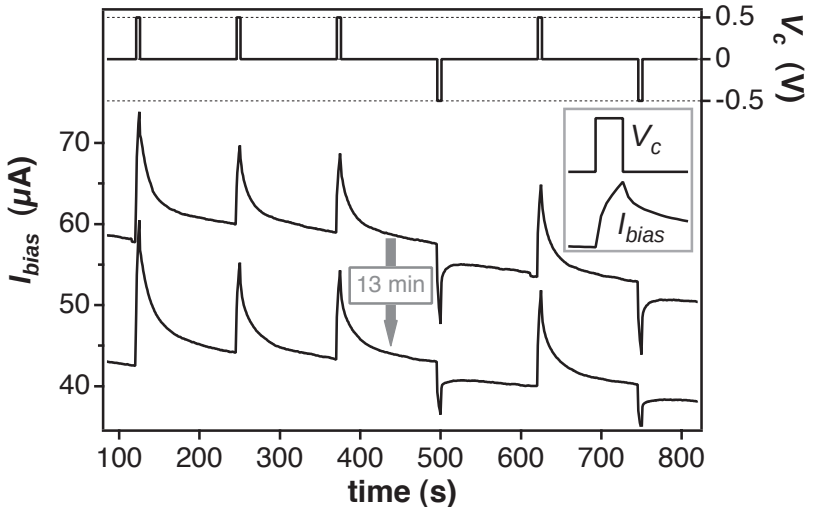

Figure 4.4: I_{bias} (raw data) versus time in response to $V_c = \pm 0.5$ V (vs SCE) pulses of 5 s duration, spaced 120 s apart. The electrolyte solution was $0.2M$ $TBAClO_4$. The plot cuts off the first 100 s during which the system was left to equilibrate. The inset shows detail of I_{bias} rise and fall for a positive V_c pulse (5 s in duration).

from the electrolyte solution. Both result in irreversible oxidation of the PPy. In the case of evaporation, the loss of solvent results in an increased salt concentration, leading to irreversible oxidation of the PPy by covalent bonding of the counterions. The presence of oxygen (*i.e.*, free OH^-) can also cause irreversible covalent bonding.[12]

With each positive V_c pulse (5 s duration), I_{bias} rises during the pulse, then relaxes to a current greater than before the pulse (vice versa for negative V_c pulses). Examining the lower of the two traces in Fig. 4.4, we first divide out the overall decay using an exponential fit ($\tau = 4984$ s) to the data past 800 s, most of which is not shown in the figure, to account for the steady oxidation referred to above. Each peak was then fit with a double exponential,

$$f(t) = A + B\,e^{-(t-t_0)/\tau_1} + C\,e^{-(t-t_0)/\tau_2}. \tag{4.1}$$

The motivation for this function arises from the two ion diffusive processes at work: the counterions at the polymer/solution interface quickly migrate away (τ_1, fast), while the counterions within the polymer bulk must make their way to this interface (τ_2, slow) before migrating away along the concentration gradient in solution. The change in current ΔI was calculated by comparing these fits extrapolated out to 800 s, an arbitrary time chosen after the last V_c pulse (Fig. 4.5 and Table 4.1):

$$\Delta I = \left[I_{after}^{800} - I_{before}^{800}\right] / I_{before}^{800}, \tag{4.2}$$

where I_{before}^{800} is the current at 800 s extrapolated from the fit *before* the V_c pulse, and I_{after}^{800} is the current at 800 s extrapolated from the fit *after* the V_c pulse (Fig. 4.5).

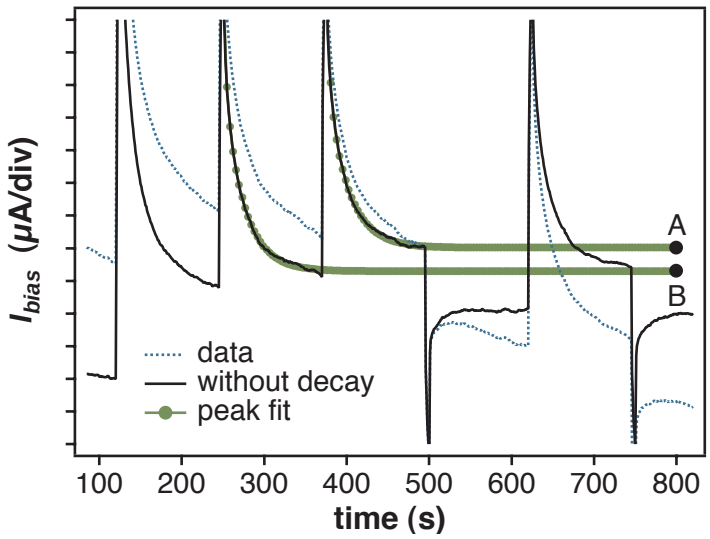

Figure 4.5: Data with overall decay subtracted and double-exponential fits to peaks 2 and 3. The two dashed lines illustrate the calculation of ΔI: point A is I_{after}^{800} and point B is I_{before}^{800}, so that $\Delta I = \frac{I(\mathrm{A})-I(\mathrm{B})}{I(\mathrm{B})}$ for peak 3. The scale on I_{bias} is 1 μA/division.

The results of the ΔI calculations (Table 4.1) show that $V_c = +0.8$ V (vs SCE) pulses increase I_{bias} by $\sim$2%–7%, and $V_c = -0.8$ V (vs SCE) pulses decrease I_{bias} by $\sim$4%. Peak

Table 4.1: Extrapolated percent changes in I_{bias} from Fig. 4.5. The peaks are numbered with increasing time. B/C is in reference to the fit parameters of Eqn. 4.1; it is the ratio of carriers associated with fast decay, B, and slow decay, C.

peak	τ_1[a] (s)	τ_2[b] (s)	B/C[c]	ΔI[d] (%)
1	11.3	49.0	1.76	+7.0
2	3.2	24.0	0.42	+2.1
3	3.7	24.8	0.45	+1.7
4	0.6	13.5	0.44	−4.4
5	3.0	23.0	0.42	+3.3
6	1.1	17.1	0.45	−3.6

[a] average error ±0.2
[b] average error ±0.8
[c] average error ±0.04
[d] average error (for peaks 2–6) ±0.05

1 is unique in both ΔI and its τ_i's since it is the response to the first V_c pulse after 2 min of equilibration. Peaks 2 and 3 are qualitatively similar and peak 5 stands out in its ΔI because it was preceded by a conductivity reducing negative V_c pulse. The two negative peaks (4 and 6) are also qualitatively similar, with peak 4 showing a larger ΔI since it followed three positive V_c pulses rather than one. With each successive V_c pulse, the polymer is nearing a saturation of counterions. Thus, a limiting of response with successive positive pulses is observed: $\Delta I_{peak1} > \Delta I_{peak2} > \Delta I_{peak3}$.

The above data were for a $0.2M$ $TBAClO_4$ solution. The response is quantitatively different in $0.2M$ NaTS electrolyte (Fig. 4.6). Most notably, the τ_i's are shorter due to the difference in size between the TS^- and ClO_4^- anions (Fig. 4.7). The increased ΔI is explained both by the higher mobility of the smaller anions and the increased strength of the gating pulses ($V_c = 2$ V vs SCE): more anions are incorporated into the polymer film with each gating pulse. The decrease in ΔI with successive V_c pulses is again observed.

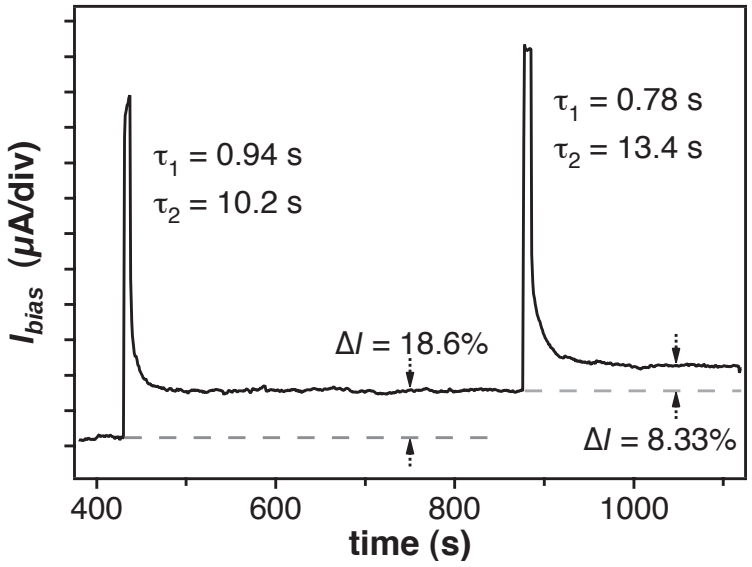

Figure 4.6: I_{bias} versus time in response to $V_c = 2$ V (vs SCE) pulses of 5 s duration in 0.2 M NaTS electrolyte solution. An exponential decay ($\tau = 3046$ s) has been subtracted from the data.

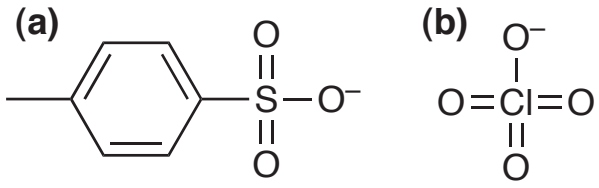

Figure 4.7: Formulas of (a) *p*-toluenesulfonate (TS^-) and (b) perchlorate (ClO_4^-) anions. Note that the TS^- is larger by an entire phenyl group.

4.3.2 Two-Electrode Junction Analysis

Results for the two-electrode analysis are shown in Fig. 4.8. As the ratio of thiophene in the polymerization solution increases, rectification of the junction becomes evident. Unlike previous experiments on PPy/Thio rectification,[13] this effect cannot be attributed to electrochemical changes in the polymer brought about by simple copolymerization of the pyrrole and thiophene. Since these junctions were polymerized at 1 V vs SCE, which is above the oxida-

Table 4.2: Quantitative analysis of rectification data in Fig. 4.8. Current in forward bias, I_+, is compared to current in reverse bias, I_-, at ± 2 V and ± 4 V. The larger the ratio, the more pronounced the rectification.

film	I_+/I_- (± 2 V)	I_+/I_- (± 4 V)
1:0	1.2	1.2
1:1	1.8	2.2
1:2	2.2	2.9

tion potential of pyrrole (~ 0.7 V) but below the oxidation potential of thiophene (~ 1.7 V),[14] the resulting polymer must be almost entirely composed of pyrrole.[15] At this voltage, a small amount of thiophene is polymerized,[16] but the rate is much slower than for the pyrrole. The junctions are then PPy films with embedded thiophene oligomers. During the polymerization, these oligomers are subjected to the electric field within the PPy bulk, which is roughly oriented radially outward from the MEA electrode toward the perimeter of the film (*i.e.*, toward the polymerization sites). Since the junction is completed by polymerizing the film above the O electrode until it reaches the I film, the electric field present on the completion of the junction points from the O to the I electrodes. The polarizability of oligothiophenes is well known,[17,18] but in this case, the final electric field "freezes" the polarization of the oligomers caused by trapped charge in the form of (bi)polarons, as discussed above. These polarized oligomers remain aligned with the final polymerization field and either enhance (forward bias) or partially cancel (reverse bias) the fields applied to the junction during analysis. The quantitative results of this rectification are shown in Table 4.2. The slight rectification observed in the 1:0 film is attributed to a small number of trapped pyrrole oligomers.

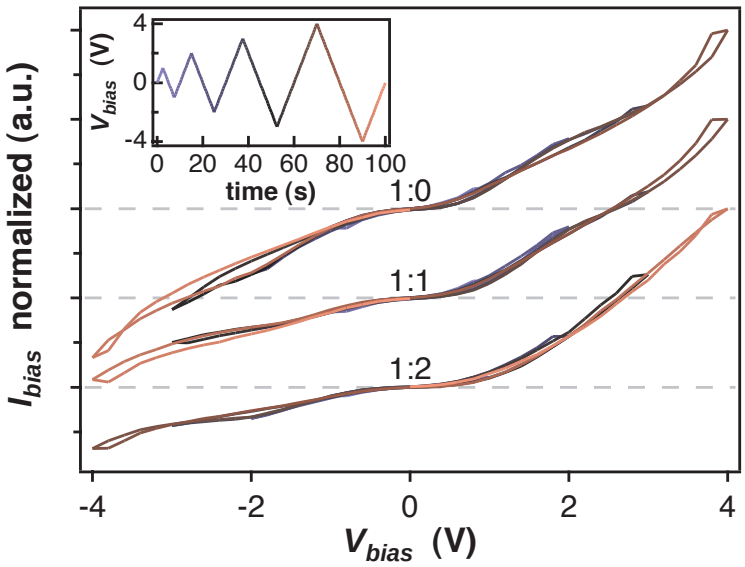

Figure 4.8: Typical current versus voltage for PPy and PPy/Thio blend two-electrode junctions. The current is normalized to the maximum positive current and the data is shifted vertically for clarity; the dotted lines represent zero current for each trace. The labels indicate the pyrrole:thiophene ratio used in the electropolymerization of the junctions. The inset shows the increasing ramp (400 mV/s) V_{bias} versus time. The color range from pale blue to pale red indicates the progression of time.

4.4 Conclusion

Simple conducting polymer junctions, as reported in this article, can be utilized for the modeling and analysis of neural systems. We have demonstrated that microscale junctions are easily patterned using commercially available microelectrode arrays and that larger networks could thus be synthesized *in situ* in an intricate connect-the-dots fashion. We have also shown that by means of an integrated control electrode, these junctions can be electrochemically weighted. In an extended network of such junctions, this individual weighting could lead to system memory. Finally, we have provided evidence of the nonlinear (in this case, rectifying) current versus voltage characteristics required for these junctions to function as elements in

complicated neural circuits. The simple two- and three-electrode junctions demonstrated here are a first step toward the fabrication of larger networks of many such junctions. The essential qualities of patternability, signal weighting, and nonlinearity, indicate that such networks would mimic the basic features of algorithmic – or even biological – neural networks, and elucidate the dynamics of these systems which emerge as the number of individual elements increases.

Acknowledgment

This research was funded by a grant from the National Science Foundation (Electrical and Communication Systems grant No. 0101794).

References

[1] A. J. Heeger, S. Kivelson, and J. Schrieffer. Solitons in conducing polymers. *Reviews of Modern Physics* **60**, 781 (1988).

[2] F. Rosenblatt. The perceptron: A probabilistic model for information storage and organization in the brain. *Psychological Review* **62**, 386 (1958).

[3] D. E. Rumelhart, G. E. Hinton, and R. J. Williams. *Parallel Distributed Processing*, MIT Press, Cambridge, MA, vol. 1, chap. Learning Internal Representations by Error Propagation, pp. 318–362 (1986).

[4] D. E. Rumelhart, G. E. Hinton, and J. L. McClelland. *Parallel Distributed Processing*, MIT Press, Cambridge, MA, vol. 1, chap. A General Framework for Parallel Distributed Processing, pp. 45–76 (1986).

[5] K. Yoshino, T. Kuwabara, and T. Kawai. Learning effect in the doping process of conducting polymer. *Japanese Journal of Applied Physics Part 2-Letters* **29** (1990).

[6] M. Fujii, T. Takahashi, H. Ihori, K. Arii, and K. Yoshino. Fundamental properties of neuron-like conducting polymer. *Synthetic Metals* **101**, 397 (1999).

[7] A. F. Diaz, J. I. Castillo, J. A. Logan, and W. Y. Lee. Electrochemistry of conducting polypyrrole films. *Journal of Electroanalytical Chemistry* **129**, 115 (1981).

[8] G. P. Kittlesen, H. S. White, and M. S. Wrighton. Chemical derivatization of microelectrode arrays by oxidation of pyrrole and n-methylpyrrole - fabrication of molecule-based electronic devices. *Journal of the American Chemical Society* **106**, 7389 (1984).

[9] X. Y. Cui and D. C. Martin. Electrochemical deposition and characterization of poly(3,4-ethylenedioxythiophene) on neural microelectrode arrays. *Sensors and Actuators, B* **89**, 92 (2003).

[10] T. Kawai, H. Motobayashi, T. Kuwabara, and K. Yoshino. An electrochemical model of neural network formation with conducting polymer by electrochemical polymerization. *Japanese Journal of Applied Physics Part 2-Letters* **30**, L622 (1991).

[11] W. P. Su, J. R. Schrieffer, and A. J. Heeger. Soliton excitations in polyacetylene. *Physical Review B* **22**, 2099 (1980).

[12] F. Beck, P. Braun, and M. Oberst. Organic electrochemistry in the solid state-overoxidation of polypyrrole. *Berichte der Bunsen-Gesellschaft Physical Chemistry* **91**, 967 (1987).

[13] M. Fujii, N. Takahashi, H. Ohnishi, and K. Yoshino. Two types of neuron-like conduct polymer prepared electrochemically and their properties. *Synthetic Metals* **85**, 1409 (1997).

[14] H. Siegerman. Appendix: Oxidation and reduction half-wave potentials fo organic compounds. In *Techniques of Chemistry*, John Wiley & Sons, New York, vol. V, p. 667 (1975).

[15] S. Kuwabata, S. Ito, and H. Yoneyama. Copolymerization of pyrrole and thiophene by electrochemical oxidation and electrochemical behavior of the resulting copolymers **135**, 1691 (1988).

[16] G. Tourillon and F. Garnier. New electrochemically generated organic conducting polymers. *Journal of Electroanalytical Chemistry* **135**, 173 (1982).

[17] M.-T. Zhao, B. P. Singh, and P. N. Prasad. A systematic study of polarizability and microscopic third-order optical nonlinearity in thiophene oligomers. *Journal of Chemical Physics* **89**, 5535 (1988).

[18] B. Champagne, D. H. Mosley, and J.-M. André. Theoretical ab initio investigation of the dipole polarizabilities of oligothiophenes and polythiophene. *Journal of Chemical Physics* **100**, 2034 (1994).

Chapter 5

Admittance Spectroscopy of Polymer-Nanoparticle Nonvolatile Memory Devices[†]

Abstract

Nonvolatile resistive memory consisting of gold nanoparticles embedded in the conducting polymer ploy(4-*n*-hexylphenyldiphenylamine) are examined using admittance spectroscopy. The frequency dependence of the devices indicates space-charge-limited transport in the high-conductivity "on" state, as well as evidence for similar transport in the lower-conductivity "off" state. Furthermore, the larger dc capacitance of the on state indicates that a greater amount of filling of the midgap nanoparticle trap levels increases the overall device conductivity, leading to the memory effect.

[†]Reprinted with permission from: D.T. Simon, M.S. Griffo, R.A. DiPietro, S.A. Swanson, and S.A. Carter, *Applied Physics Letters* **89**, 133510 (2006). Copyright 2006, American Institute of Physics. [doi: 10.1063/1.2357560]

5.1 Introduction

The demand for faster, cheaper, denser memory technology and the accelerating pace of the semiconductor industry have driven an expansion of information storage research. In addition to novel approaches to scaling of existing technology,[1–3] candidates for entirely different storage media are being investigated. In particular, several solid-state nonvolatile low power consumption structures are being actively pursued, *e.g.*, magnetic random access memory,[4] ferroelectric random access memory,[5] phase-change (ovonic unified memory),[6] and polymeric/organic.[7–11] Many of these structures leverage a two-terminal-per-bit cross-point architecture to simplify the fabrication process and reduce the effective footprint of each bit.

Nonvolatile memory based on metallic nanoparticles embedded in a polymer host has been suggested[8,9] as one of these new cross-point memory structures. In this system, trap levels situated within the band gap of the polymer are introduced by the nanoparticles. It has been theorized that the memory effect is due to the charge state of these traps but the exact relationship between this charge state and the device conductivity remains unclear. As these midgap traps should affect the frequency response of the device, we have applied the techniques of admittance spectroscopy to elucidate the correlation between device conductivity and the introduction of metallic nanoparticle trap states.

5.2 Experiment

In this letter, we focus on devices consisting of a blend of triphenylphosphine-protected Au nanoparticles ($\sim$4 nm diameter) (AuNP) and the crosslinkable conducting polymer poly(4-

n-hexylphenyldiphenylamine) (*x*HTPA) sandwiched between Al electrodes (as reported by Bozano *et al.*[12]). Using a shadow mask, a 10 nm seed layer of Cr, followed by 30 nm Al electrode was thermally evaporated onto a glass substrate at about 10^{-6} torr. The substrates were then removed from vacuum, and a 1.74 wt % *x*HTPA:xylenes solution loaded with 2.5 wt % AuNP:*x*HTPA was spin cast at 500 rpm for 10 s, followed by 800 rpm for 30 s, resulting in a 125 nm thick active layer. This *x*HTPA:AuNP layer was then annealed at 150 °C for 1 h to remove the solvent and crosslink the polymer. The devices were then returned to vacuum, and a top 30 nm Al electrode was evaporated. All fabrication and characterization was carried out under nitrogen.

The measurements were performed using a WaveTek 650 variable phase synthesizer to source a voltage across the device and a load resistor in series. When performing the dc current versus voltage (*I*-*V*) sweeps, a Keithley 2010 Multimeter measured the voltage drop across the load resistor to get the dc current. During the frequency sweeps, a Stanford Research Systems SR830 lock-in amplifier measured the voltage drop and phase shift across the load resistor. Dividing the ac current measured across the load resistor by the input voltage yields the complex admittance, $Y = I/V = G(\omega) + i\omega C(\omega)$, the real and imaginary parts of which give the conductance $G(\omega)$ and capacitance $C(\omega)$.[†] The input voltage for all frequency sweeps consisted of 50 mV rms ac signal with a 1 V dc bias, chosen to be at or near the expected "read" voltage. Low temperature measurements were conducted in an Oxford Instruments MagLab System 2000 cryostat.

[†] $C(\omega)$ accounts for all complex contributions to the admittance: capacitive and inductive. However, it can be assumed that inductive behavior is negligible at the frequencies used and with the device architecture employed.

5.3 Results and Discussion

5.3.1 DC Response

The results of a typical room temperature dc measurement are shown in Fig. 5.1. The device exhibits three distinct regions of current-voltage relationship: (a) below some threshold voltage, V_{TH}, at which the device switches conductance states, (b) a negative differential resistance (NDR) region, (c) the region beyond NDR. Using a read voltage $< V_{TH}$, at least two stable states are observed, which will be referred to in this letter as "on" – high conductivity – and "off" – low conductivity. The device can be set from off to on by applying a voltage equal to, or slightly greater than, V_{TH}, and set from on to off by application of a voltage near the end of the NDR region. Past NDR, the current appears to continue on a trend extending from the off state, which indicates that the same mode of conduction might be at play in these two regions.

It should be noted that the on-off current ratio of less than 1 order of magnitude in this device structure (Fig. 5.1a) is low in comparison to devices employing other polymer hosts. For example, poly(2-methoxy-5-(2′-ethylhexyloxy)-*p*-phenylene vinylene) (MEH-PPV) yielded on-off ratios ranging from 1 to 4 orders of magnitude (Fig. 5.1b). This effect may be due to the cross-linkable nature of *x*HTPA: the end groups intended for cross-linking may introduce sufficient trap sites to blur the distinction between the on and off states. Note that in Fig. 5.1(a), the averaged current of similarly prepared devices without NPs is below the off state of the NP-containing memory device, yet well above the off state of the MEH-PPV:AuNP device. However, the *x*HTPA device structure had the highest yield and resulted in the largest amount of collected data, therefore impedance measurements were performed on this structure.

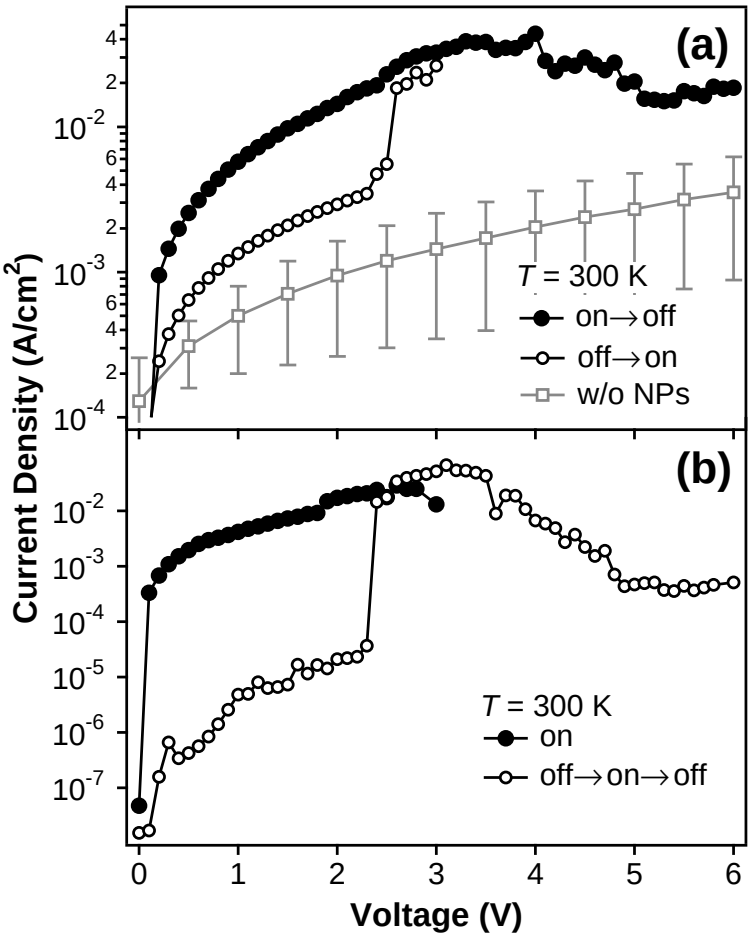

Figure 5.1: Characteristic current versus voltage curves at room temperature exhibiting the bistable memory effect using (a) an Al/*x*HTPA:AuNP/Al structure and (b) a Au/MEH-PPV:AuNP/Au structure. In both cases the device is set on by sweeping past V_{TH} (here, ≈ 2.5 V), and off by continuing the sweep into the negative differential resistance region. The gray curve in (a) shows the average response (and standard errors) of a similar "clean" *x*HTPA structure without NPs.

5.3.2 AC Response

The Cole-Cole plot of the impedance in the on and off states is shown in Fig. 5.2. The off state appears roughly semicircular, indicating that the device behaves somewhat as a parallel *RC* circuit. However, the on state shows a marked deviation from semicircular at low

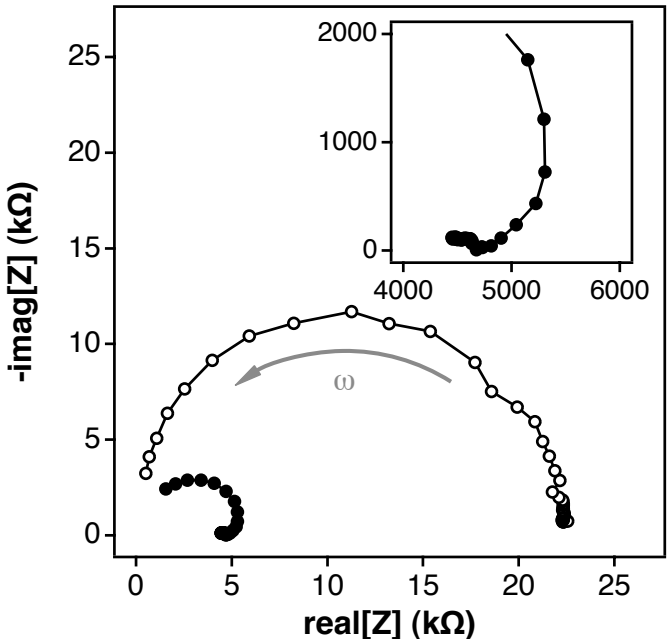

Figure 5.2: Cole-Cole plot of imaginary versus real impedance for (●) on and (○) off states. The arrow indicates the direction of increasing frequency. The inset is a zoom showing the inductive bend (*i.e.*, deviation from semicircle) in the on state which corresponds to the negative peak in Fig. 5.3.

frequency, indicating that the *RC* equivalent is not valid. The corresponding capacitance and conductance versus frequency are shown in Fig. 5.3. At low frequency, the capacitance in the on state is larger than in the off state. Given the presence of trap states, this greater ability to store charge indicates that these traps are more likely to be filled in the on state. The faster fall off of the on state capacitance with frequency is further evidence that a larger amount of charge – located at the interfaces, in the bulk, or both – cannot as easily keep up with the applied ac field. Finally, the presence of a negative (inductive) peak in the on state capacitance is indicative of space-charge-limited (SCL) behavior (cf. Fig. 5.3 and Refs. 14–16). The dips in the conductance of both the on and off state also qualitatively match SCL behavior. Following

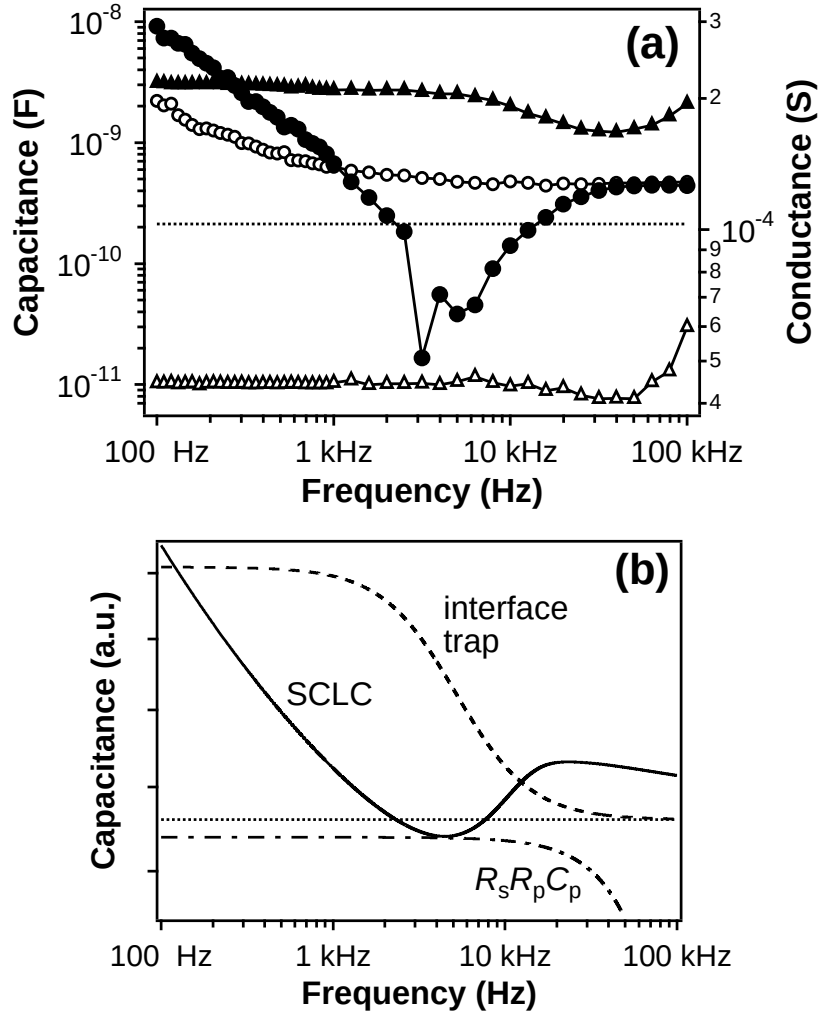

Figure 5.3: (a) Capacitance and conductance as a function of frequency: (●) on state capacitance; (▲) on state conductance; (○) off state capacitance; (△) off state conductance. (b) Capacitance versus frequency for three device models: interfacial trap layers (Ref. 13), space-charge limited current (Ref. 14), and a resistor in series with a parallel resistor-capacitor combination ($R_sR_pC_p$). The horizontal dotted line in both plots shows the geometric capacitance, $C_{geo} = 212$ pF.

the analysis of Martens *et al.*,[14] the dc mobility can then be found using the time-of-flight

argument, $\mu_{dc} = L^2/(\tau_t V)$, for thickness L, transit time $\tau_t = 1/f_{peak}$, and dc bias V.[†] Applying this equation to the on-state peak in Fig. 5.3(a), $\mu_{dc} = 7.2 \times 10^{-7}$ cm^2/V s at 1 V bias.

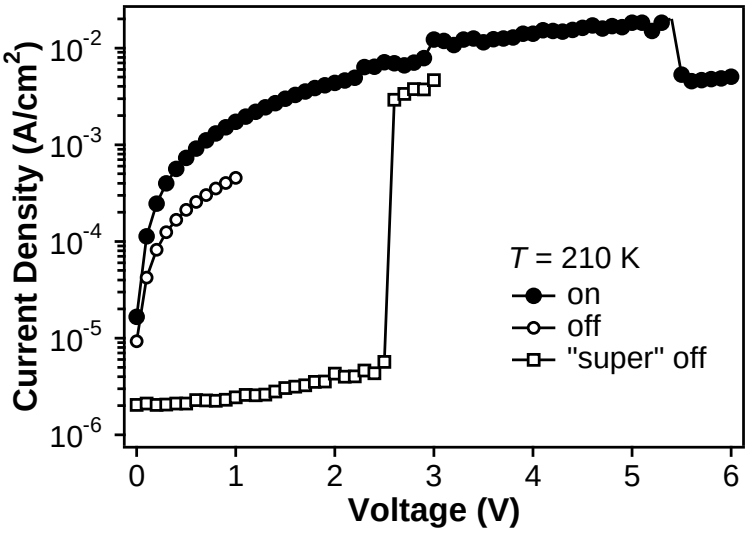

Figure 5.4: Typical current versus voltage curves at low temperature (in this plot, 210 K). The on and off curves shown here are in the same current density range as is observed at room temperatures. However, the super off state appears (sporadically) only at suppressed temperature. The labels, on, off, and super off indicate the state of the device at the beginning of the (positive) voltage sweep.

5.3.3 Low-Temperature Response

At room temperature the characteristic sharp increase in conductivity at V_{TH} occurs consistently at ∼2.5 V and the NDR is observed over the range of ∼ 3–5 V. On subjecting the device to low temperature (110 K – 250 K) all device characteristics – location of V_{TH}, sharpness of switch at V_{TH}, and width of NDR – became sporadic or broadened. The V_{TH} occurred over ∼ 1.5–3 V (but was still mostly sharp) and the NDR region often narrowed to

[†]This is simply a statement that the carrier velocity $v = \mu_{dc}E = L/\tau_t$, where E is the electric field in the device. Using the approximation $E = V/L$ and solving for μ_{dc}, one gets $\mu_{dc} = L^2/(\tau_t V)$.

< 1 V in width. This instability at low temperature did not affect the current density of the on/off states previously observed at room temperature (Fig. 5.4). This indicates that conduction in both on and off is dominated by NP-assisted tunneling and not typical conjugated polymer conduction [as further evidenced by the off state in Fig. 5.1(a) having a higher current than the "clean" *x*HTPA devices]. Furthermore, a "super" off state was observed which exhibits a very low current as expected for a clean semiconducting polymer at cryogenic temperature.[17]

5.4 Mechanism and Conclusion

The above data suggest a possible mechanism. In the voltage region below V_{TH}, the conductivity of the device is determined by the amount of charge trapped on the NPs. These relatively immobilized charges create a space-charge region which reduces the injection barrier, thus increasing the device conductivity. In contrast to the usual effect of space charge on current, this *increase* in conductivity is due to the build up of charge of opposite sign to the injected charge. At higher bias, some of the trapped charge is either swept away by the field, or eliminated by recombination, leading to NDR.

Analysis of the frequency-dependent capacitance of multiple on and off states suggest the high current may be related to an increase in space charge due to trapped charge on the NPs. These data also imply that trap sites in the polymer are critical to optimization of device performance and lead to the possibility of decreasing the off state current by using purified or highly ordered polymers.

Acknowledgments

The authors wish to thank J. Campbell Scott, Luisa Bozano, and Glenn Alers for valuable assistance. This research was funded by a grant from the National Science Foundation (Electrical and Communication Systems grant No. 0101794).

References

[1] N. C. C. Lu. Advanced cell structures for dynamic rams. *IEEE Circuits and Devices Magazine* **5**, 27 (1989).

[2] B. Eitan, P. Pavan, I. Bloom, E. Aloni, A. Frommer, and D. Finzi. NROM: A novel localized trapping, 2-bit nonvolatile memory cell. *IEEE Electron Device Letters* **21**, 543 (2000).

[3] J. De Blauwe. Nanocrystal nonvolatile memory devices. *IEEE Transactions on Nanotechnology* **1**, 72 (2002).

[4] J. Akerman. Toward a universal memory. *Science* **308**, 508 (2005).

[5] A. Sheikholeslami and P. G. Gulak. A survey of circuit innovations in ferroelectric random-access memories. *Proceedings of the IEEE* **88**, 667 (2000).

[6] S. Hudgens and B. Johnson. Overview of phase-change chalcogenide nonvolatile memory technology. *MRS Bulletin* **29**, 829 (2004).

[7] L. P. Ma, J. Liu, and Y. Yang. Organic electrical bistable devices and rewritable memory cells. *Applied Physics Letters* **80**, 2997 (2002).

[8] J. Ouyang, C.-W. Chu, C. R. Szmanda, L. Ma, and Y. Yang. Programmable polymer thin film and non-volatile memory device. *Nature Materials* **3**, 918 (2004).

[9] L. D. Bozano, B. W. Kean, V. R. Deline, J. R. Salem, and J. C. Scott. Mechanism for bistability in organic memory elements. *Applied Physics Letters* **84**, 607 (2004).

[10] M. Lauters, B. McCarthy, D. Sarid, and G. E. Jabbour. Nonvolatile multilevel conductance and memory effects in organic thin films. *Applied Physics Letters* **87**, 231105 (2005).

[11] M. Cölle, M. Büchel, and D. M. de Leeuw. Switching and filamentary conduction in non-volatile organic memories. *Organic Electronics* **7** (2006).

[12] L. D. Bozano, B. W. Kean, M. Beinhoff, K. R. Carter, P. M. Rice, and J. C. Scott. Organic materials and thin-film structures for cross-point memory cells based on trapping in metallic nanoparticles. *Advanced Functional Materials* **15**, 1933 (2005).

[13] E. H. Nicollian and J. R. Brews. *MOS (Metal Oxide Semiconductor) Physics and Technology*. Wiley-Interscience, New York (1982).

[14] H. C. F. Martens, H. B. Brom, and P. W. M. Blom. Frequency-dependent electrical response of holes in poly(p-phenylene vinylene). *Physical Review B* **60**, R8489 (1999).

[15] S. Berleb and W. Brütting. Dispersive electron transport in tris(8-hydroxyquinoline) aluminum (Alq_3) probed by impedance spectroscopy. *Physical Review Letters* **89**, 286601 (2002).

[16] H. H. P. Gommans, M. Kemerink, G. G. Andersson, and R. M. T. Pijper. Charge transport and trapping in Cs-doped poly(dialkoxy-p-phenylene vinylene) light-emitting diodes. *Physical Review B* **69**, 155216 (2004).

[17] L. Bozano, S. E. Tuttle, S. A. Carter, and P. J. Brock. Temperature-dependent recombination in polymer composite light-emitting diodes. *Applied Physics Letters* **73**, 3911 (1998).

Chapter 6

Fixed *p-i-n* Junction Polymer Light-emitting Electrochemical Cells Based on Charged Self-assembled Monolayers[†]

Abstract

The authors report on enhanced efficiency of polymer light-emitting electrochemical cells (LECs) by means of forming an *n*-doping self-assembled monolayer (SAM) at the cathode-polymer interface. The addition of the SAM, a silane-based salt with structural similarity to the commonly used LEC *n*-dopant tetra-*n*-butylammonium, caused a twofold increase in quantum efficiency. Photovoltaic analysis indicates that the SAM increases both the open-circuit voltage and short-circuit current. Current versus voltage data are presented which indicate that the SAM does not simply introduce an interfacial dipole layer, but rather provides a fixed doping region, and thus a more stable *p-i-n* structure.

[†]Reprinted with permission from: D.T. Simon, D. B. Stanislowski, and S.A. Carter, *Applied Physics Letters* **90**, 103508 (2007). Copyright 2007, American Institute of Physics. [doi: 10.1063/1.2711769]

6.1 Introduction

Polymer light-emitting electrochemical cells (LECs) have been given much attention in recent years as an enhancement over the simpler polymer light-emitting diode (LED).[1–3] These devices differ from the standard polymer LED structure[4,5] in that the active polymer layer is blended with "doping" counterions and a solid polymer electrolyte. When a bias is applied across the device, charge is created within the polymer by oxidation/reduction of the conjugated backbone. The counterions migrate toward the electrodes and stabilize ("dope") the polymer charge, thereby creating *p*- and *n*-doped regions at the anode and cathode, respectively, and leaving a relatively undoped intrinsic region in the middle. The resulting *p*-*i*-*n* structure has the advantage over the standard polymer LED of higher conductivity at the doped interfaces, enabling a larger amount of charge to be injected and radiatively recombine in the central insulating region.

The trade-off for this enhancement is that it takes time to move the ions and establish the *p*-*i*-*n* junction.[6–8] Furthermore, when the bias is removed, the ions forming the junction migrate away from the interfaces and back toward a neutral position within the bulk of the device. For this reason, several methods have been devised to stabilize the junction in the absence of bias, among them, "frozen" junctions,[6,9,10] where the *p*-*i*-*n* structure is formed at elevated temperature and then fixed at suppressed temperature, and additional polymer electrolyte/counterion layers near the interfaces[11] to fix the regions where dopants can be found.

Another method, presented below, is to fix the *p*-*i*-*n* structure by covalently attaching the dopant ions – in the form of a self-assembled monolayer (SAM) – to one of the interfaces.

A similar method has been used to increase efficiency of small-molecule organic LEDs,[12,13] but in these cases the effect is attributed to dipolar effects of the SAM and increased wettability of the modified substrate. The effect discussed below differs in that an interfacial dipole layer is insufficient to explain the data, leading to the conclusion that the SAM is electrochemically doping the polymer host.

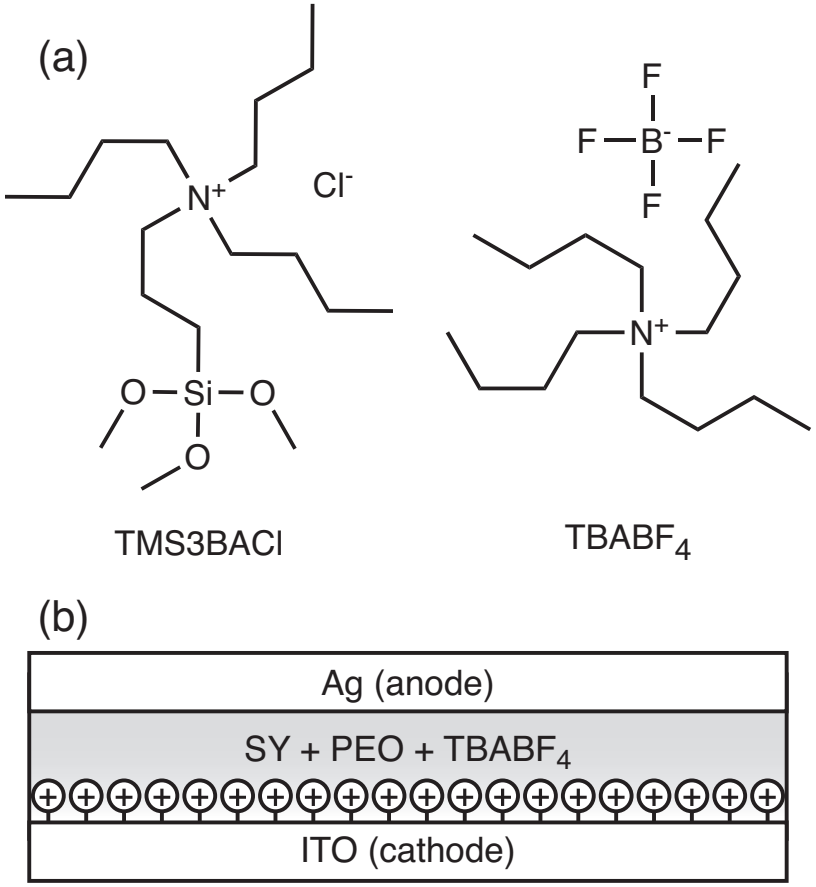

Figure 6.1: (a) Chemical structures of TMS3BACl and $TBABF_4$ (note the similarity of the cations). (b) Device structure of SAM-based LEC, where the cation comprising the SAM is $TMS3BA^+$.

In this letter, we employ this SAM-based *p-i-n* structure using a LEC active layer (described below) sandwiched between a Ag anode and SAM-modified indium-tin oxide (ITO)

cathode (Fig. 6.1). We present quantum efficiency vs. time, and current and luminance vs. time on this structure with and without the SAM. We also discuss an analogous LED structure with and without the SAM.

6.2 Experiment

LEC devices were prepared using a 0.8 wt % solution of the conducing polymer Super Yellow (SY, Covion/Merck) in chlorobenzene plus 33 wt % of the polymer electrolyte poly(ethyleneoxide) (PEO, 5×10^6 M.W., PolySciences) and 8 wt % of the dopant tetra-*n*-butylammonium tetrafluoroborate ($TBABF_4$, Alfa Aesar), where these last two weight percentages are relative to the polymer. Clean LED devices were also prepared using a 0.5 wt % solution of SY in chlorobenzene. Formation of the *n*-doping SAM was performed by soaking UV-plasma treated substrates in a 5.75 wt % solution of trimethoxysilylpropyl-tri-*n*-butylammonium chloride ($TMS3BA^+ \cdot Cl^-$ = TMS3BACl, Gelest) in methanol for 24 h at room temperature. The LED or LEC layer was spun from solution either directly on the ITO surface or on the SAM-modified ITO, then annealed at 140 °C for 30 min in vacuum, yielding thicknesses of 110 nm (LED) and 300 nm (LEC). A top electrode of Ag was deposited by thermal evaporation at a vacuum of about 10^{-6} torr. The final LEC device structure is shown in Fig. 6.1. Characterization was performed using a Keithley 2400 source meter for current and voltage sourcing and measuring, and a photodiode attached to a Keithley 485 picoammeter to measure electroluminescence. An Oriel xenon arc lamp was used as a solar simulator for photocurrent/photovoltaic analysis. The devices were stored and tested in nitrogen.

6.3 Results and Discussion

6.3.1 Photovoltaic Analysis of LED Structure

As a base line for the effect of the SAM, the LED architectures of ITO/SY/Ag and ITO/SAM/SY/Ag were examined. Typical current versus voltage (*I-V*) curves in the dark and under solar illumination are shown in Fig. 6.2, the data are summarized in Table 6.1. Data were obtained by sweeping voltage from 0 V to some positive voltage, back through 0 V to the same negative voltage, then back to 0 V with a sweep rate of $\sim$80 mV/s (no SAM) or $\sim$350 mV/s (with SAM). The positive-to-negative sweeps are shown as they were characteristic of both sweep directions. The data show a strong effect of adding the SAM, *i.e.*, the suppression of the dark current, and increase in open-circuit voltage V_{oc} in dark *and* solar illuminated situations. The large V_{oc} observed in the dark with the SAM – which varied in the range of -300 to -900 mV between devices and tended to increase slightly with multiple sweeps in rapid succession – can be attributed to migration of the Cl^- ions of the TMS3BACl and the slow return of these ions to the SAM interface. Under forward bias, the Cl^- ions are forced toward the ITO interface, canceling the charge on the $TMS3BA^+$ SAM, and thereby quenching its *n*-doping effect. In reverse bias, the Cl^- ions are forced away from the ITO interface, allowing the $TMS3BA^+$ to *n* dope the polymer. The observed V_{oc} in the dark with the SAM is then an artifact of an internal field caused by the arrangement of positive ($TMS3BA^+$) and negative (Cl^-) charge.

The suppression of current in forward bias, most notably in the dark, is also evidence that the effect of the SAM is not simply to add a dipole layer at the interface. Numerous

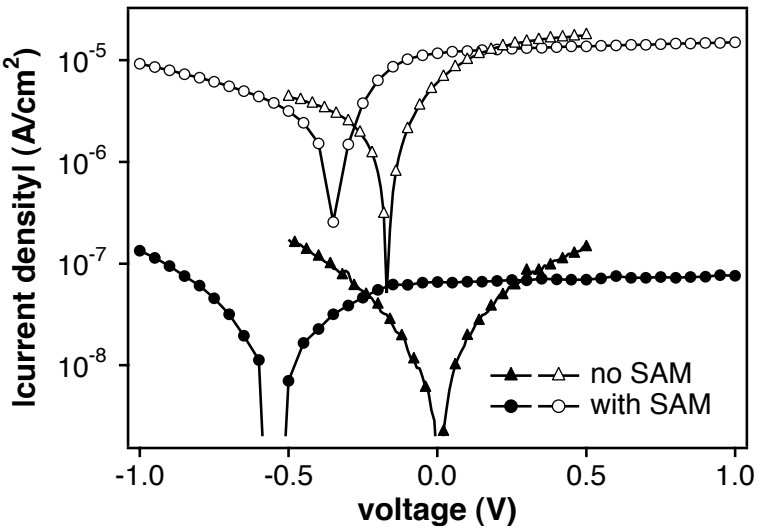

Figure 6.2: Current versus voltage data for ITO/SY/Ag (triangles) and ITO/SAM/SY/Ag (circles). The closed symbols indicate dark current, and the open symbols indicate current under solar illumination.

Table 6.1: Summary of photovoltaic data for ITO/SY/Ag and ITO/SAM/SY/Ag structures (as shown in Fig. 6.2).

	Illum.	V_{oc} (mV)	I_{sc} (μA/cm^2)	Fill factor (%)
Without SAM	Solar	-168	6.09	22
With SAM	Dark	-550[a]	0.0661	32
	Solar	-342	11.7	33

[a] SAM dark V_{oc}'s varied among different devices in the range -300 to -900 mV.

researchers have investigated the effects of small-molecule monolayers on the work function of ITO.[12–17] Unlike the materials chosen by these other researchers, TMS3BACl can become a charged – and therefore doping – species under bias. Using semi-empirical Hartree-Fock optimization via the PM3 Hamiltonian, the component of the dipole moment perpendicular to the ITO surface was calculated to be -6.8 D for TMS3BA$^+$, and $+8.6$ D for TMS3BACl, where the perpendicular direction was chosen parallel to the Si–N direction (cf. Fig. 6.1) and pointing away from the ITO. Following the usual electrostatic dipole layer argument,[12,18] the

positive dipole in forward bias, when the Cl^- ions are present, should *decrease* the barrier to hole injection and enhance forward bias current. Instead, current is suppressed, indicating that the SAM's role must be other than a simple dipole layer. Given the argument of the previous paragraph, and the structural similarity to the dopant $TBABF_4$ (Fig. 6.1), the data suggest that the SAM is *n* doping the polymer in reverse bias.

A final note on the data shown in Fig. 6.2 is that the consistent negative V_{oc} indicates that the effective work function arrangement is such that the ITO is the preferred electron injector. While electron injection from ITO is contrary to the standard LED/LEC,[5] it is consistent within the wide range of reported work functions for ITO [4.3–5.1 eV (Ref. 19)] and Ag [4.52–4.74 eV (Ref. 20)].

6.3.2 Quantum Efficiency Analysis of LEC Structure

Due to the dynamic nature of the active material, the first experiment that each LEC device was subjected to was constant-current stressing, thus "forming" the devices by arranging the internal ions into the *p-i-n* (or *n-i-p*) structure and yielding quantum efficiency (QE) as a function of time. Typical QE versus time for the LEC architecture with and without the SAM is shown in Fig. 6.3. The devices show a "native" QE before stressing: 2% with the SAM, compared to 1% without the SAM. On stressing the devices at $+$ or -3.33 mA/cm^2, both structures show divergence from this native QE. The negative stress (ITO as electron injector) resulted in an increase and stabilization in QE, whereas the positive stress (ITO as hole injector) resulted in decay of QE toward zero. This behavior indicates that regardless of the SAM, there is a preferred polarity: ITO as cathode, and Ag as anode, similar to the results shown in Fig. 6.2

for the LED structure. In reverse bias, TMS3BA$^+$ and TBA$^+$ are pushed toward the ITO, both of which *n* dope the polymer, facilitating electron injection. However, in forward bias, Cl^-, as well as BF_4^- in the LEC, are pushed toward the ITO, quenching the *n* doping of the SAM. The decay in light emission in forward bias is different from previously reported LECs,[2,9] but was consistently observed for our devices. This may be due to luminescence quenching by a high concentration of TBA$^+$ ions at the Ag interface; it has been observed that high salt concentration leads to a decrease in electroluminescence. The twofold enhancement in QE is then due to the combined doping of the SAM and the LEC salt. Note that the data presented in Fig. 6.3 are from the initial current stressing for each of these devices.

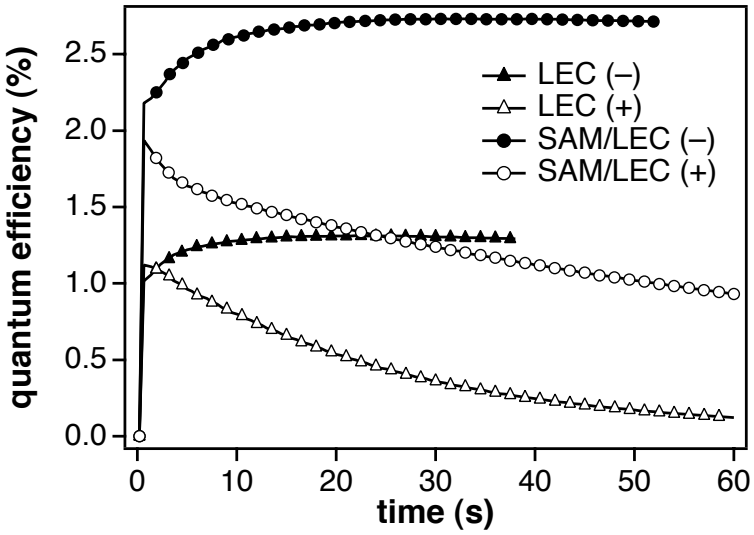

Figure 6.3: Quantum efficiency for ITO/LEC/Ag (triangles) and ITO/SAM/LEC/Ag (circles). The + and − signs indicate that the data were taken at constant current density of + or -3.33 mA/cm^2.

6.3.3 Current and Light vs Voltage Analysis of LEC Structure

Current and luminance versus voltage (*I-L-V*) data were obtained by sweeping voltage from 0 V toward some positive or negative voltage (chosen as the point at which the current would reach ≈3.33 mA/cm^2), back through 0–1 V of the opposite polarity, then back to zero. In this way, the data represent the *I-L-V* response of a given forming direction: the reverse bias sweeps represent the case of active *n* doping at the ITO, whereas forward bias sweeps represent the case of quenched *n* doping at the ITO. Characteristic LEC *I-L-V* response is shown in Fig. 6.4, where the data are from the second of the three sweep directions described above (*i.e.*, with the devices formed). The data indicate that in both biases, the current is lower and luminance higher for the devices with the SAM. In reverse bias, the *n* doping at the ITO interface not only increases electron injection, but also acts as a hole blocking layer. Thus holes attempting to escape into the ITO are blocked at the interface and recombine with injected electrons, increasing light emission but decreasing current. In forward bias, the data suggest that there is a greater imbalance in injected charge, most likely in favor of hole injection from the ITO (given the relative work functions of ITO and Ag), resulting in the noticeable decrease in light emission. As with the LED response (Fig. 6.2), the presence of the SAM suppresses current. However, the SAM still increases light emission, possibly as a result of continued blocking/balancing of injected charge – even considering the quenched SAM doping.

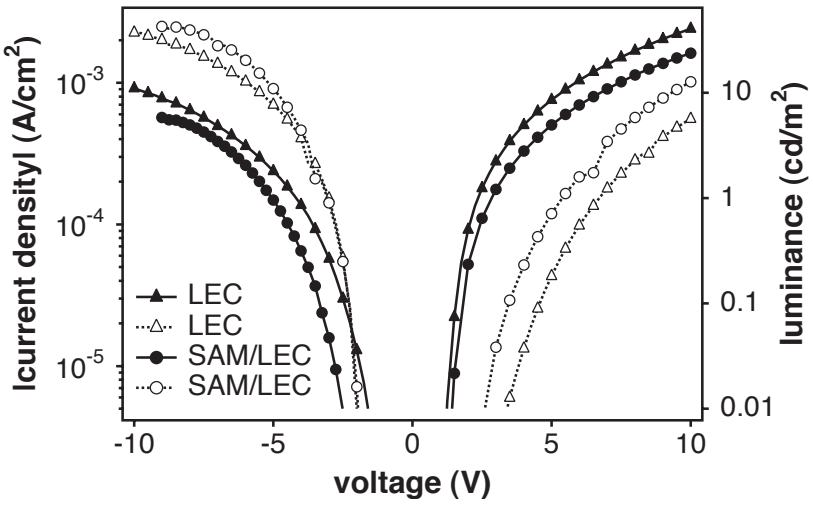

Figure 6.4: Current and luminance versus voltage (*I-L-V*) data for ITO/LEC/Ag (triangles) and ITO/SAM/LEC/Ag (circles). The closed symbols indicate current density, while the open symbols indicate luminance. Note that the data in each bias are from a different set of voltage sweeps on different devices (*e.g.*, the LEC data does not represent a single sweep from -10 to $+10$ V, but rather one sweep from -10 to 0 V, and another from $+10$ to 0 V, on different devices).

6.4 Conclusion

The LEC devices presented in this letter based on charged SAM-modified ITO electrodes show increased quantum efficiency compared to analogous devices on bare ITO. Similar polymer-only (LED) devices show an increase in open-circuit voltage and short-circuit current under solar illumination, leading to a higher photovoltaic fill factor than their bare ITO analogs. These gains are at little expense in that the SAM preparation is easily carried out both in a laboratory environment or in high-throughput production by simple soaking.

These results warrant continued study and optimization of the basic structure. In particular, the SAM material for this research was chosen based on commercial availability and chemical similarity to one of many commonly used LEC dopant ions (Fig. 6.1). Other

SAM materials, forming layers at either – or both – of the polymer/electrode interfaces could be feasibly employed. Furthermore, the SAM material presented above has only a propyl link ($\lesssim$ 1 nm) between the silane head group and charged tail group. One interesting possibility would be to use SAM materials – or polymeric materials – with a significantly longer link, providing fixed *n* and/or *p* doping deeper into the bulk of the device.

Acknowledgments

The authors wish to thank Jian Ping Chen for his assistance throughout this project. This research was funded by a Small Business Technology Transfer Grant from the National Science Foundation (USA, Award No. 0539802) in conjunction with Add-Vision, Incorporated, Scotts Valley, California.

References

[1] Q. Pei, G. Yu, C. Zhang, Y. Yang, and A. J. Heeger. Polymer light-emitting electrochemical cells. *Science* **269**, 1086 (1995).

[2] Q. Pei, Y. Yang, G. Yu, C. Zhang, and A. Heeger. Polymer light-emitting electrochemical cells: In situ formation of a light-emitting p-n junction. *Journal of the American Chemical Society* **118**, 3922 (1996).

[3] L. Edman. Bringing light to solid-state electrolytes: The polymer light-emitting electrochemical cell. *Electrochimica Acta* **50**, 3878 (2005).

[4] J. H. Burroughes, D. D. C. Bradley, A. R. Brown, R. N. Marks, K. Mackay, R. H. Friend, P. L. Burns, and A. B. Holmes. Light-emitting diodes based on conjugated polymers. *Nature* **347**, 539 (1990).

[5] R. H. Friend, R. W. Gymer, A. B. Holmes, J. H. Burroughes, R. N. Marks, C. Taliani, D. D. C. Bradley, D. A. D. Santos, J. L. Bredas, M. Logdlund, and W. R. Salaneck. Electroluminescence in conjugated polymers. *Nature* **397**, 121 (1999).

[6] J. Gao, G. Yu, and A. J. Heeger. Polymer light-emitting electrochemical cells with frozen p-i-n junction. *Applied Physics Letters* **71**, 1293 (1997).

[7] L. Edman, M. A. Summers, S. K. Buratto, and A. J. Heeger. Polymer light-emitting electrochemical cells: Doping, luminescence, and mobility. *Physical Review B* **70**, 115212 (2004).

[8] J. Dane, C. Tracy, and J. Gao. Direct observation of a frozen junction in polymer light-emitting electrochemical cells. *Applied Physics Letters* **86**, 153509 (2005).

[9] J. Gao, Y. Li, G. Yu, and A. J. Heeger. Polymer light-emitting electrochemical cells with frozen junctions. *Journal of Applied Physics* **86**, 4594 (1999).

[10] J.-H. Shin, S. Xiao, A. Fransson, and L. Edman. Polymer light-emitting electrochemical cells: Frozen-junction operation of an "ionic liquid" device. *Applied Physics Letters* **87**, 043506 (2005).

[11] T.-W. Lee, H.-C. Lee, and O. O. Park. High-efficiency polymer light-emitting devices using organic salts: A multilayer structure to improve light-emitting electrochemical cells. *Applied Physics Letters* **81**, 214 (2002).

[12] S. F. J. Appleyard, S. R. Day, R. D. Pickford, and M. R. Willis. Organic electroluminescent devices: enhanced carrier injection using sam derivatized ito electrodes. *Journal of Materials Chemistry* **10**, 169 (2000).

[13] J. Lee, B.-J. Jung, J.-I. Lee, H. Y. Chu, L.-M. Do, and H.-K. Shim. Modification of an ito anode with a hole-transporting sam for improved oled device characteristics. *Journal of Materials Chemistry* **12**, 3494 (2002).

[14] N. Karsi, P. Lang, M. Chehimi, M. Delamar, and G. Horowitz. Modification of indium tin oxide films by alkanethiol and fatty acid self-assembled monolayers: A comparative study. *Langmuir* **22**, 3118 (2006).

[15] E. Bruner, N. Koch, A. Span, S. Bernasek, A. Kahn, and J. Schwartz. Controlling the work function of indium tin oxide: Differentiating dipolar from local surface effects. *Journal of the American Chemical Society* **124**, 3192 (2002).

[16] R. A. Hatton, S. R. Day, M. A. Chesters, and M. R. Willis. Organic electroluminescent devices: enhanced carrier injection using an organosilane self assembled monolayer (sam) derivatized ito electrode. *Thin Solid Films* **394**, 291 (2001).

[17] W. Osikowicz, X. Crispin, C. Tengstedt, L. Lindell, T. Kugler, and W. R. Salaneck. Transparent low-work-function indium tin oxide electrode obtained by molecular scale interface engineering. *Applied Physics Letters* **85**, 1616 (2004).

[18] H. Ishii, K. Sugiyama, E. Ito, and K. Seki. Energy level alignment and interfacial electronic structures at organic/metal and organic/organic interfaces. *Advanced Materials* **11**, 605 (1999).

[19] J. S. Kim, B. Lagel, E. Moons, N. Johansson, I. D. Baikie, W. R. Salaneck, R. H. Friend, and F. Cacialli. Kelvin probe and ultraviolet photoemission measurements of indium tin oxide work function: a comparison. *Synthetic Metals* **111-112**, 311 (2000).

[20] D. R. Lide, ed. *CRC Handbook of Chemistry and Physics*, CRC Press, Boca Raton, Florida, p. 12.114. 87 edn. (2006).

Appendix A

List of Symbols and Acronyms

$\boldsymbol{\Phi_m}$ — metallic work function

ac — alternating current

CCD — charge-coupled device

CE — counter electrode

dc — direct current

DUT — device under test

$\boldsymbol{E_f}$ — Fermi energy

$\boldsymbol{e}$ — elementary electronic charge, 1.60218×10^{-19} C

FF — fill factor

GPIB — general purpose interface bus

GUI — graphical user interface

HOMO — highest occupied molecular orbital

I-L-V — current and light (or luminance) versus voltage

I-V — current versus voltage

$\boldsymbol{I_{sc}}$ — short-circuit current

IS — impedance (or immitance) spectroscopy

ITO — indium-tin oxide

LEC — light-emitting electrochemical device (or cell)

LED — light-emitting diode

LUMO — lowest unoccupied molecular orbital

MEA — microelectrode (or multielectrode) array

MEH-PPV — poly(2-methoxy-5-(2′-ethylhexyloxy)-*p*-phenylene vinylene)

NDR — negative differential resistance

NP — nanoparticle

OLED — organic light-emitting diode

PA — polyacetylene

PEDOT-PSS — poly(3,4-ethylenedioxythiophene) poly(styrenesulfonate)

PEO — poly(ethyleneoxide)

PE — power efficiency

PLED — polymer light-emitting diode

PPV — poly(*p*-phenylene vinylene)

PPy — polypyrrole

PT — polythiophene

QE — quantum efficiency

RE — reference electrode

SCE — saturated calomel electrode

SCL — space-charge limited

SHE — standard hydrogen electrode

SMU — source meter unit

SY — Super Yellow (proprietary PPV-derived conducting polymer)

TMS3BA — trimethoxysilane-tri-*n*-butylammonium

V-L-T — voltage and light (or luminance) versus time

$\boldsymbol{V_{oc}}$ — open-circuit voltage

WE — working electrode

Appendix B

Software-Hardware Interfacing via the General Purpose Interface Bus (GPIB)

All modern experimental science requires the acquisition and storage of large amounts of data. In practice, the task of recording readouts from measurement equipment cannot be done "by hand" – due to the speed of acquisition, the sheer volume of information, or both – and a computer interface must be employed to assist the researcher. While many instruments have a proprietary or custom software-hardware interface, the majority of high-precision instrumentation available today has the ability to interface with personal computers via what is known as the General Purpose Interface Bus (GPIB). GPIB, also known as IEEE (Institute of Electrical and Electronics Engineers) Standard 488,[1,2] refers to both the physical connections and wires, and to the standardized software interface.

Physically, GPIB allows up to fifteen devices to be connected to a single computer. The devices generally come with a GPIB interface (port) built in, while the computer often requires an expansion card (*e.g.*, a PCI card) to add the port. Various software packages, such a LabView, Igor Pro and MatLab, can then access the GPIB interface, and thus communicate with the various devices, each of which are assigned a unique "GPIB address".

The simplicity of GPIB lies in the software interface. Commands and data go back and forth the the measurement equipment as text strings. In theory, any command or series of commands that could be individually typed into the instrument through its physical interface can be sent rapidly over GPIB. For example, a series of commands in the Igor Pro procedural language might be:

```
SndStrng(24,":SOURCE:VOLT:START 0")
SndStrng(24,":SOURCE:VOLT:STOP 10")
SndStrng(24,":SOURCE:VOLT:STEP 0.1")
SndStrng(24,":SOURCE:VOLT:MODE SWEEP")
SndStrng(24,":OUTPUT ON; :INIT")
```

where the Igor Pro function `SndStrng()` takes two arguments. The first is the GPIB address to send the text command to, and the second is the actual string to send. Here, a Keithley 2400 SourceMeter at GPIB address 24 is being sent five lines of code setting up a voltage sweep from 0 to 10 V in steps of 0.1 V. Note that the last line of code shows the use of the semicolon for putting two commands into the same string. Using four more semicolons, the above example could have been sent to the device using a single `SndStrng()` command.

Retrieving data from instrumentation also consists of passing text strings. Data download is initiated from the computer side: a query command is sent to the instrument, and the instrument responds with a formatted string. For example, a string such as `"0, 0, 0.1, 0.001, 0.2, 0.008, 0.3, 0.027,..."` might contain sequential pairs of voltage and current points. This string can then be parsed by the software into tables or traces of the data – here an *I*-*V* sweep.

A final note about the implementation of GPIB is in regard to the so-called "service request". All communication must be initiated by the computer, so experiment timing can become an issue. For example, a program such as MultiSweep (described in detail in App. C) must wait for a given voltage sweep to complete before requesting data from the Keithley 2400. How does it know how long to wait, or when to request the data? This problem is solved by the service request. During initialization, a program such as MultiSweep would command the Keithley 2400 to create a service request on completion of a given task (in this case a voltage sweep). The software can then be "put on hold" by being told to wait for a service request before proceeding. The final caveat is that the service request is not instrument specific, it is global on the GPIB network. Thus, in the above example, for MultiSweep to wait properly for the Keithley 2400 to complete the sweep (and create the service request), no other service requests from any other equipment can be initiated during the sweep.

For more information on GPIB, the reader is referred to the references below, in particular Ref. 3, as well as the product manuals for the various instruments in question.

The system used to acquire the data in this manuscript consisted of a National Instruments PCI-GPIB expansion card in an Apple PowerMac G4 desktop computer running the Igor Pro software package.

References

[1] *IEEE 488.1: Higher performance protocol for the standard digital interface for programmable instrumentation – Part 1: General*. IEC 60488-1(E) (2004).

[2] *IEEE 488.2: Standard digital interface for programmable instrumentation – Part 2: Codes, formats, protocols and common commands*. IEC 60488-2(E) (2004).

[3] *NI-488.2 User Manual*. National Instruments Corporation, 370428C-01 edn. (2005).

Appendix C

MultiSweep: A Configurable Software Interface for Voltage Sweep Data Acquisition

During the course of the research that led to Chaps. 5 and 6, a software package was developed that could handle automated acquisition of *I-V*, *I-L-V*, and concurrent *I-V* and impedance spectroscopy data. The program, MultiSweep, was written in the Igor Pro (WaveMetrics, Inc.) procedural language, leveraging the graphical interface of Igor Pro with the hardware interfacing of GPIB (cf. App. B). The name MultiSweep is meant to signify that the program can perform any number of sequential arbitrary current vs. voltage acquisition sweeps. Over the course of development, many additional features were added to the program, most notably the ability to perform impedance spectroscopy measurements, and photocurrent measurements.[†]

In its simplest form, MultiSweep performs basic *I-V* measurements as described in Sec. 3.3 above. To do this, the step-measure delay is specified in the graphical user interface (GUI) within Igor Pro (Fig. C.1) and the various voltage sweeps are specified in a tab-delimited text file of the form,

[†]Additional features, including electrode multiplexing and photovoltaic analysis, were also included, but are not documented here.

$$\begin{array}{ccc} V_{i1} & V_{f1} & \Delta V_1 \\ V_{i2} & V_{f2} & \Delta V_2 \\ \vdots & \vdots & \vdots \\ V_{in} & V_{fn} & \Delta V_n. \end{array}$$

MultiSweep then steps through the input file, commanding a Keithley 2400 SourceMeter to perform the voltage sweep specified. For basic *I-V* measurements, this process is controlled by the Keithley 2400: MultiSweep simply specifies the starting and stopping voltages (V_i and V_f, respectively), the voltage step (ΔV), and the step-measure delay. The Keithley 2400 then performs the sweep automatically, measuring the current at each voltage point (after waiting for the step-measure delay). At the end of each sweep, the data is downloaded to the computer, and the next sweep is initiated.

In its more complicated incarnations, additional measurement hardware is required. In the case of impedance spectroscopy measurement, a WaveTek 650 universal source is used for sourcing ac, dc, or combination ac+dc voltage, and the current is measured by a Stanford Research System SR830 lockin amplifier (ac component) and a Keithley 2010 multimeter (dc component) as described in Sec. 3.4. For the case of electroluminescent photocurrent measurement, MultiSweep retrieves the current through a silicon photodiode attached to the DUT via a Keithley 485 picoammeter.

If temperature dependent measurements are desired, MultiSweep can control an Oxford Instruments MagLab System 2000 cryostat. In this case, input lines of the form

$$T_i \quad [dummy] \quad T_{eqb,i}$$

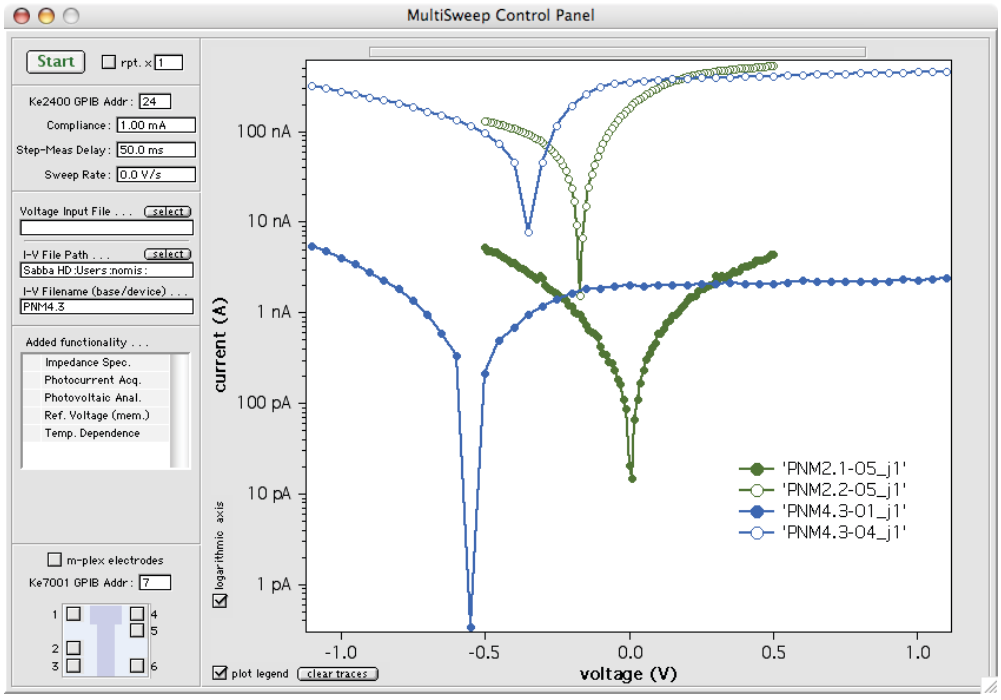

Figure C.1: Main control panel of the MultiSweep GUI. On the left are controls specifying the input files and parameters. On the right is the readout display (with sample data).

in the sweep input file indicate that the temperature should be set to T_i (in K), and the system should equilibrate for $T_{eqb,i}$ minutes. The $[dummy]$ is simply a placeholder which can be equal to anything. These input lines can be interspersed between voltage sweep lines. For all types of measurement functionality, Fig. C.2 below shows the programmatic methodology.

In any case, MultiSweep communicates back and forth with the equipment via text messages passed through GPIB. Outgoing (command) messages are generated by concatenating text strings and variables within the program. For example, to set the voltage on the Keithley 2400, a command such as

```
SndStrng(A,"SOURCE:VOLT " + num2str(Vi))
```

```
get acquisition type and parameters from GUI and sweep input file
if impedance spectroscopy measurement then
    initialize WaveTek 650 voltage source
    initialize SR830 lockin amplifier
    initialize Keithley 2010 multimeter
else
    initialize Keithley 2400 SourceMeter
if temperature dependent measurement then
    initialize Oxford cryostat
if photocurrent (I-L-V) measurement then
    initialize Keithley 485 picoammeter
foreach line of the sweep input file do
    if temperature line then
        set temperature on Oxford cryostat
        wait for temperature equilibration time
    else if impedance spectroscopy measurement then
        foreach voltage point calculated from V_i, V_f, and ΔV do
            set voltage on WaveTek 650
            measure current from Keithley 2010
        foreach frequency point do
            set frequency of WaveTek 650
            measure ac signal from SR830
            measure dc signal from Keithley 2010
        display data in GUI
    else
        send sweep parameters to Keithley 2400
        if photocurrent measurement then
            foreach voltage point calculated from V_i, V_f, and ΔV do
                set voltage on Keithley 2400
                measure current from Keithley 2400
                measure photocurrent from Keithley 485
        else
            set Keithley 2400 to perform automatic sweep
            download I-V data for entire sweep from Keithley 2400
        display data in GUI
save data to file
```

Figure C.2: The basic algorithm for the data acquistion program MultiSweep.

might be issued, where `SndStrng()` is the general function for sending text strings through GPIB, `A` is a numeric variable containing the GPIB address of the Keithley 2400, `num2str()` is a function that converts numeric variables into strings, and `Vi` is a numeric variable equal to the voltage being set. For more details on GPIB, see App. B.